Inferring the oriented elastic tensor from surface wave observations: Preliminary application across the Western US

Journal:	*Geophysical Journal International*
Manuscript ID:	GJI-S-14-0727
Manuscript Type:	Research Paper
Date Submitted by the Author:	14-Sep-2014
Complete List of Authors:	Xie, Jiayi; University of Colorado at Boulder, Physics Ritzwoller, Michael; University of Colorado Boulder, Physics Brownlee, Sarah; Wayne State University, Geology Hacker, Bradley; Geological Sciences,
Keywords:	Seismic anisotropy < SEISMOLOGY, Crustal structure < TECTONOPHYSICS, Surface waves and free oscillations < SEISMOLOGY

Inferring the oriented elastic tensor from surface wave observations: Preliminary application across the Western US

Jiayi Xie[1], Michael H. Ritzwoller[1], S.J. Brownlee[2], and B.R. Hacker[3]

1 – Center for Imaging the Earth's Interior, Department of Physics, University of Colorado at Boulder, Boulder, CO 80309-0390, USA (jiayi.xie@colorado.edu)
2 – Department of Geology, Wayne State University, Detroit, MI 48202
3 – Department of Earth Science, UC Santa Barbara, CA USA 93106-9630

Abstract

Radial and azimuthal anisotropy in seismic wave speeds have long been observed using surface waves and are believed to be controlled by earlier episodes of deformation within the Earth's crust and uppermost mantle. Although radial and azimuthal anisotropy reflect important aspects of anisotropic media, few studies have tried to interpret them jointly. We describe a method of inversion that reconciles simultaneous observations of radial and azimuthal anisotropy under the assumption of a hexagonally symmetric elastic tensor with a tilted symmetry axis defined by dip and strike angles. We show that observations of radial anisotropy and the 2ψ component of azimuthal anisotropy for Rayleigh waves obtained using USArray data in the western US can be fit well under this assumption. Our inferences occur within the framework of a Bayesian Monte Carlo inversion, which yields a posterior distribution that reflects both variances of and covariances between all model variables. Principal results include the following: (1) Inherent S-wave anisotropy (γ) is fairly homogeneous vertically across the crust, on average, and spatially across the western US. (2) Averaging over the region of study and in depth, γ in the crust is approximately 4.1%±2%. (3) There are two distinct groups of models in the posterior distribution in which the strike angle of anisotropy in the crust (defined by the intersection of the foliation plane with earth's surface) is approximately orthogonal between the two sets. (4) γ in the crust is approximately the same in the two groups of models. (5) Dip angles in the two groups of models show similar spatial variability and display geological coherence. (6) However, Rayleigh wave fast axis directions are orthogonal to strike angle in the geologically preferred group of models. (7) The estimated dip angle may be interpreted in two ways: as a measure of the actual dip of the foliation of anisotropic material within the crust, or as a proxy for another non-geometric variable, most likely a measure of the deviation from hexagonal symmetry of the medium. (8) Tilting the symmetry axis of an anisotropic medium produces apparent radial and apparent azimuthal

anisotropies that are both smaller in amplitude than the inherent anisotropy of the medium, which means that most previous studies have probably underestimated the strength of anisotropy.

1. Introduction

The study of anisotropy using surface waves is primarily of interest to seismologists because surface waves provide a homogenous sampling of the Earth's crust and uppermost mantle over large areas. For this reason, robust inferences about anisotropy from surface waves are typically not restricted to small regions, which provides the possibility to draw conclusions broadly over a variety of geologic and tectonic settings (e.g., *Anderson and Regan,* 1983; *Ekström and Dziewoński*, 1998; *Gung et al*., 2003; *Smith et al*., 2004; *Kustowski et al*., 2008; *Nettles and Dziewoński*, 2008). Cross-correlations of ambient noise principally present relatively short and intermediate period surface waves for interpretation. Therefore, the introduction of ambient noise tomography into the set of standard seismological methods has allowed for increasingly detailed information to be gained about the crust (e.g., *Shapiro et al*., 2005; *Yao et al*., 2006; *Bensen et al*., 2009; *Moschetti et al*., 2010a; *Ritzwoller et al*., 2011; *Yang et al*., 2012; *Ekström*, 2013), and information about anisotropy that is deriving from ambient noise is mainly crustal in origin (e.g., *Huang et al*., 2010; *Moschetti et al*., 2010b; *Yao et al*., 2010; *Lin et al*., 2011; *Xie et al*., 2013). In this paper, surface waves from both ambient noise and earthquakes will be used, and the principal focus will be on crustal anisotropy.

Studies of seismic anisotropy using surface waves primarily take two forms. In the first, azimuthally averaged (transversely isotropic) Rayleigh and Love wave travel time curves are studied to determine if they are consistent with an isotropic medium of propagation. If not, radial anisotropy (or polarization anisotropy) is introduced to the medium to resolve what is often called the "Rayleigh-Love discrepancy". In the second form, the directional dependence of surface wave travel times is used to determine azimuthal anisotropy. In both

cases, the anisotropy is typically interpreted to result from the mechanism of formation of the medium, either through (1) the crystallographic or lattice preferred orientation of anisotropic minerals (*Christensen*, 1984; *Ribe*, 1992) or (2) the anisotropic shape distribution of isotropic materials, such as laminated structure (*Backus*, 1962; *Kawakatsu et al*., 2009) or fluid filled cracks (*Anderson et al*., 1974; *Crampin*, 1984; *Babuška*, 1991). Indeed, one of the principal motivations to study seismic anisotropy is to understand the deformation that a medium was subject to during its formation and evolution.

Irrespective of the physical cause or causes of the anisotropy, however, assumptions are typically (and necessarily) made to aid in and simplify the inference from surface wave observations to information about the elastic tensor, which governs the propagation of surface waves and generates the observed anisotropy. In studies of radial anisotropy (e.g., *Dziewoński and Anderson*, 1981; *Moschetti et al*., 2010b; *Xie et al*., 2013), the typical assumption is that the medium is transversely isotropic or possesses hexagonal symmetry with a vertical symmetry axis ($\hat{z}$-axis in **Fig. 1**). Such a medium is defined by five depth-dependent elastic parameters (A, C, N, L, F or η), where A and C are compressional moduli and N and L are shear moduli. In this case, the 6x6 elastic modulus matrix, $C_{\alpha\beta}$, the Voigt simplification of the elastic tensor, can be written as the following symmetric matrix:

$$ {}^{V}C_{\alpha\beta} = \begin{bmatrix} A & A-2N & F & 0 & 0 & 0 \\ A-2N & A & F & 0 & 0 & 0 \\ F & F & C & 0 & 0 & 0 \\ 0 & 0 & 0 & L & 0 & 0 \\ 0 & 0 & 0 & 0 & L & 0 \\ 0 & 0 & 0 & 0 & 0 & N \end{bmatrix} \quad (1) $$

where η = F/(A-2L) and the superscript V stands for vertical symmetry axis. With a vertical symmetry axis, a hexagonally symmetric medium will produce no azimuthal variation in

surface wave speeds mainly because the C_{44} and C_{55} matrix elements are identical. In addition, because N is frequently greater than L in earth material, $C_{66} > C_{44}$. This is referred to as positive S-wave radial anisotropy and implies that Love waves are faster than predicted from an isotropic medium that fits Rayleigh wave speeds. In contrast, studies of azimuthal anisotropy (e.g., *Simons et al.*, 2002; *Marone and Romanowicz*, 2007; *Yao et al.*, 2010; *Lin et al.*, 2011) may implicitly interpret the medium to have a horizontal symmetry axis ($\hat{x}$-axis in **Fig. 1**). In the case of hexagonal symmetry, the elastic modulus matrix has the following form:

$$ {}^{H}C_{\alpha\beta} = \begin{bmatrix} C & F & F & 0 & 0 & 0 \\ F & A & A-2N & 0 & 0 & 0 \\ F & A-2N & A & 0 & 0 & 0 \\ 0 & 0 & 0 & N & 0 & 0 \\ 0 & 0 & 0 & 0 & L & 0 \\ 0 & 0 & 0 & 0 & 0 & L \end{bmatrix} \qquad (2) $$

The fact that N is typically larger than L implies that $C_{66} < C_{44}$, which is referred to as negative S-wave radial anisotropy and is observed in the mantle beneath the mid-ocean ridges (e.g., *Ekström and Dziewoński*, 1998; *Zhou et al*., 2006; *Nettles and Dziewoński,* 2008) and is observed only rarely in the crust (e.g., *Xie et al*., 2013). Also, mainly because $C_{44} \neq C_{55}$, this elastic tensor will generate azimuthal variations in wave speeds. These assumptions of vertical and horizontal symmetry are obviously in conflict with one another and cannot explain the widely observed co-existence of positive radial anisotropy and azimuthal anisotropy (e.g., *Huang et al*., 2010; *Yao et al*., 2010; *Yuan and Romanowicz*, 2010; *Yuan et al*., 2011; *Xie et al*., 2013; *Hacker et al., 2014*).

The anisotropic properties of an elastic medium and the anisotropy of seismic wave speeds depend both on the detailed constitution of the elastic tensor and on its orientation.

Observational studies that have not explicitly considered the orientation of the elasticity tensor (perhaps by assuming either a vertical or horizontal symmetry axis) produce estimates of radial and azimuthal anisotropy, respectively, that we refer to as "apparent", because the real symmetry axis of the medium (assuming it exists) may differ from horizontal or vertical. Observations of apparent anisotropy, therefore, depend on the unknown orientation of the medium, which limits the usefulness of such observations to constrain the elastic properties of the medium. Ultimately, in order to understand the anisotropy that seismic waves exhibit, it is important to seek information about the (depth-dependent) elastic tensor within the crust and mantle together with its orientation. We refer to the anisotropic properties of a medium as "inherent anisotropy" only when they are measured (or inferred) for the untilted hexagonally symmetric elastic tensor. We use the term "inherent" as opposed to "intrinsic" anisotropy because the latter term often refers to anisotropy that results from a specific cause, namely, from crystal orientation (*Wang et al*., 2013; *Anderson and Thomsen*, 2015). Further discussion of the distinction between apparent and inherent anisotropy takes place later in the paper.

The purpose of this paper is to describe a method to reconcile simultaneous observations of radial and azimuthal anisotropy under the assumption of a hexagonally symmetric elastic tensor with a tilted symmetry axis (**Figure 1a**), as was first suggested by *Montagner and Nataf* (1988). Such an assumption has been applied before to body wave observations (e.g., *Okaya and McEvilly*, 2003) as well as studies of the effect of mode-coupling on surface waves (e.g., *Yu and Park*, 1993). Applications here are made using Rayleigh and Love wave dispersion maps from the western US obtained using the Transportable Array (TA) stations from EarthScope USArray. We obtain isotropic Rayleigh wave phase speed maps from 8 to

40 sec period from ambient noise data and from 24 to 90 sec period from earthquake data. Isotropic Love wave maps are taken from ambient noise data from 10 to 25 sec period and from earthquake data from 24 to 50 sec period. These observations produce azimuthally isotropic Rayleigh and Love wave phase speed curves at each point on a 0.2°x0.2° grid across the study region. The 2ψ Rayleigh wave azimuthal anisotropy data are obtained from 10 to 40 sec from ambient noise data and 24 to 60 sec period from earthquake data, where ψ is the azimuth of propagation of the wave. No azimuthal anisotropy data from Love waves are used in this study. Love wave azimuthal variations are expected (and observed) to display dominantly 4ψ azimuthal variation, which is a much more difficult observation to make than the 2ψ azimuthal variation of Rayleigh waves.

The assumption of hexagonal symmetry is a starting point designed to reduce the number of free parameters that govern the anisotropic medium, which simplifies and accelerates the inverse problem. To describe the medium under this assumption at a given depth requires seven unknowns, the five moduli that govern the inherent characteristics of a hexagonally symmetric medium and two angles through which the elastic tensor is rotated: the dip and strike angles. There are, however, reasons to believe that crustal anisotropy, which is the primary focus of this paper, may display dominantly hexagonal symmetry. For example, strongly laminated or foliated rocks are nearly hexagonal in symmetry (*Okaya and McEvilly*, 2003) and lamination in the lower crust has been observed worldwide (*Meissner et al.*, 2006). Also, the primary anisotropic mineral in the middle crust is probably mica (*Weiss et al*., 1999; *Meissner et al*., 2006), which displays approximate hexagonal symmetry. Therefore, if anisotropy derives from the CPO of anisotropic minerals, then mid-crustal anisotropy may be well approximated by an inherently hexagonally symmetric

elastic tensor. However, as discussed later in the paper, amphiboles, which are common in the middle and lower crusts, are also strongly anisotropic but are more orthorhombic than hexagonal in symmetry (*Meissner et al*., 2006; *Tatham et al*., 2008). If amphiboles are a significant source of anisotropy, then what we estimate by assuming hexagonal symmetry may not have geologic meaning, but may yet contain information about the lower-order symmetry of the real elastic tensor, and inferences that are derived should be cognizant of this.

Two further comments will conclude this discussion. First, Rayleigh and Love waves are strongly sensitive only to four (N, L, θ, ϕ, as described later) of the seven unknowns that define a rotated hexagonally symmetric elastic medium. Therefore, a straightforward inversion for the elastic tensor is impractical using surface wave data alone. For this reason we cast the inverse problem in terms of a Bayesian Monte Carlo approach in which we estimate a range of elastic tensors that agree with the data. This allows us to estimate uncertainties in all variables as well as the covariances or correlations between them as represented by the "posterior distribution" at each location and depth. As discussed later, we find that certain elements of the elastic tensor are well determined, others are not, and the posterior distribution is bimodal in three important variables. Second, the assumption of hexagonal symmetry is actually not required for the method we present, but simplifies it significantly. We could have, for example, cast the inverse problem in terms of an un-rotated orthorhombic elastic tensor, but at the expense of introducing two additional free parameters.

In Section 2 we briefly describe the data we use and the observations from surface waves that serve as the input data for the inversion. In Section 3, we explain the theoretical

background of the inversion, concentrating on the connections between surface wave observations and elastic constants. In Sections 4 and 5, the model parameterization and inversion are discussed. Finally, in Section 6, we present the inversion results and discuss possible physical implications of the estimated models.

2. Surface wave data

This paper is motivated by the need for a new inversion method, which is described in a later section, that self-consistently interprets observations of radial and azimuthal anisotropy of surface waves. The method is applied here to surface wave data obtained in a region that encompasses the western US and part of the central US, where USArray stations operated between the years 2005 and 2010. We use continuous ambient noise data to measure Rayleigh and Love wave phase speeds between station-pairs and data from earthquakes with Mw>5.0 to generate dispersion curves between event-station pairs. We follow the tomographic methods described by *Lin et al.* (2009) and *Lin and Ritzwoller* (2011) known as eikonal and Helmholtz tomography to estimate phase velocity maps with uncertainties. Our region of study extends somewhat further eastward than these earlier studies, however, and we obtain Love wave dispersion maps in addition to Rayleigh wave maps.

At short periods, we use only ambient noise data and at very long periods only earthquake data are used, but there is an intermediate period range where ambient noise data and earthquake data are combined. The short period interval extends from 8 to 22 sec period where we apply eikonal tomography to produce the Rayleigh wave dispersion maps (*Lin et al.*, 2009). The period band of overlap of ambient noise and earthquake measurements for Rayleigh waves is broad, ranging from 24 - 40 sec period. Love wave measurements, however, only extend to 25 sec period so overlap between ambient noise and earthquake

measurements occurs only at 25 sec period. At longer periods (>40 sec for Rayleigh waves, > 25 sec for Love waves) earthquake data alone are used, with Rayleigh wave measurements extending to 90 sec period and Love wave measurements to 50 sec period. The signal-to-noise ratio is smaller at long periods for Love waves than for Rayleigh waves, which reduces the longest period that Love wave phase speed maps can be constructed. Following the recommendation of *Lin and Ritzwoller* (2011), we apply eikonal tomography up to 50 sec period but we apply Helmholtz tomography, which accounts for finite frequency effects, at periods longer than 50 sec. Also following *Lin et al*. (2009), the uncertainties in the isotropic maps are scaled up to encompass the differences between the ambient noise and earthquake-derived maps.

An example of the output of eikonal and Helmholtz tomography for a point in the Basin and Range province (Point A, **Fig. 3a**) is shown in **Figure 2** in which the local azimuthal variation of Rayleigh wave phase velocity is presented at three periods. At each period for each location a truncated Fourier series is fit to the data to estimate the azimuthal dependent of phase velocity for both Rayleigh and Love waves:

$$c(T,\psi) = c_0(T)\left[1 + a_2\cos\left(2(\psi - \varphi_{FA})\right) + a_4\cos\left(4(\psi - \alpha)\right)\right] \quad (3)$$

where T is period, ψ is the azimuth of propagation of the wave measured clockwise from north, c_0 is isotropic phase speed, φ_{FA} is what we call the 2ψ fast axis direction, α is an analogous phase angle for 4ψ variations in phase speed, and a_2 and a_4 are the relative amplitudes of the 2ψ and 4ψ anisotropy. Uncertainties in each of these quantities are determined at each location and period.

Examples of isotropic phase speed maps for Rayleigh and Love waves are presented **Figure**

3, where the short period maps (10 sec period) are determined from ambient noise, the long period maps (Rayleigh: 70 sec, Love: 45 sec) are from earthquake data, and the intermediate period maps are a combination of both data sets. Although azimuthally anisotropic phase speed maps are estimated for both Rayleigh and Love waves we use only the 2ψ maps for Rayleigh waves here. Rayleigh wave azimuthal anisotropy is observed to be dominated by 180° periodicity (or 2ψ anisotropy) as expected for slightly anisotropic media (*Simth & Dahlen*, 1973). For Love waves, we use only the azimuthally isotropic phase speed maps because Love wave anisotropy is dominated by 90° periodicity (or 4ψ anisotropy), which is a more difficult observable that we choose not to invoke. Examples of observations of Rayleigh wave azimuthal anisotropy are presented in **Figure 4** at three periods, where the length of each bar is the peak-to-peak amplitude of 2ψ anisotropy, $2a_2$, and the orientation of each bar is the fast axis direction ϕ_{FA}.

Examples of characteristic maps (Rayleigh: 32 sec period, Love: 25 sec period) of the estimated uncertainties in these quantities are presented in **Figure 5**. The spatially averaged uncertainties for the isotropic Rayleigh and Love wave speeds (**Fig. 5a,b**) are 8 m/s and 18 m/s, respectively, illustrating that Love wave uncertainties are typically more than twice as large as Rayleigh wave uncertainties. Uncertainties in the fast axis directions depend on the amplitude of azimuthal anisotropy and the regions of large uncertainty in **Figure 5c** occur where the amplitude of azimuthal anisotropy is small. The average peak-to-peak amplitude of 2ψ anisotropy for the 32 sec Rayleigh wave is approximately 0.8%, and for this amplitude the uncertainty of the fast axis direction averages about 8°. The uncertainty grows sharply as the amplitude of anisotropy reduces below about 0.5% and diminishes slowly as the amplitude grows above 1%. The average uncertainty in the amplitude of 2ψ anisotropy

for the 32 sec Rayleigh wave is about 0.24%, which is less than 1/3 of the average amplitude of anisotropy. Thus, the amplitude of the 2ψ Rayleigh wave anisotropy is determined typically to better than 3σ.

From the maps of isotropic phase speed for Rayleigh and Love waves and the amplitude and fast axis direction of 2ψ anisotropy for Rayleigh waves (and their uncertainties), we generate at each grid point in the study area isotropic phase speed curves for both Rayleigh and Love waves and 2ψ anisotropic dispersion curves for Rayleigh waves. This raw material forms the basis for the later inversion for a 3D model. **Figure 6** presents examples for the two locations (A: Basin and Range, B: Colorado Plateau identified in **Fig. 3a)** that illustrate how these curves can vary. For Point A, the fast azimuth of Rayleigh wave does not change strongly with period, but the amplitude of azimuthal anisotropy increases with period. In contrast, for Point B, the fast azimuth changes with period, but the amplitude of azimuthal anisotropy tends to decrease with period.

Similar data sets have been used previously to study the anisotropic structure of the western US. For example, *Moschetti et al*. (2010a, 2010b) used isotropic Rayleigh and Love wave phase speed dispersion curves such as those presented in **Figure 6a,d** to image apparent crustal radial anisotropy. *Lin et al*. (2011) used azimuthally anisotropic dispersion curves similar to those in **Figure 6b,c,e,f** to image the apparent crustal and uppermost mantle azimuthal anisotropy. These two data sets were interpreted separately, but here we attempt to explain both radial and azimuthal anisotropy simultaneously using tilted hexagonally symmetric media (**Fig. 1**).

3. The elastic tensor and surface wave anisotropy

In a linearly elastic medium, stress and strain are related by a linear constitutive equation,

$\sigma_{ij} = c_{ijkl}\varepsilon_{kl}$, where c_{ijkl} is the elastic tensor that describes the behavior of the medium under strain and, therefore, determines the speed of seismic waves. Without loss of generality, the elastic tensor can be compacted into the 6x6 elastic modulus matrix, $C_{\alpha\beta}$, following the Voigt recipe (e.g., *Thomsen*, 1986). Although a general elastic tensor is described by 21 elastic constants, hexagonal symmetry is often used to characterize earth materials due to its simplicity (e.g., *Dziewoński and Anderson*, 1981), and can approximate many actual situations in the Earth (e.g., laminated structures, LPO of mica or micaceous rocks, alignment of olivine crystals along the a axis with randomly oriented b and c axes). The hexagonally symmetric elastic modulus matrices with vertical ($^{V}C_{\alpha\beta}$) and horizontal ($^{H}C_{\alpha\beta}$) symmetry axes are presented in the Introduction. A general reorientation of the symmetry axis, which we call a tilt, is achieved by rotating $^{V}C_{\alpha\beta}$ through the dip and strike angles defined in **Figure 1a**, as described in the Appendix. The elastic constants for a tilted hexagonally symmetric medium can be characterized by seven independent parameters, five unique elastic constants (A, C, N, L, F) that describe the untilted hexagonally symmetric (transversely isotropic) elastic tensor, and two for the orientation of the symmetry axis.

For a model of the elastic tensor as a function of depth at a given location, the forward problem in which period and azimuth dependent Rayleigh and Love wave phase speed curves are computed is described in Appendix A. For weakly anisotropic media, surface wave velocities are only sensitive to 13 elements of the elastic tensor and the remaining 8 elements are in the null space of surface wave velocities (*Montagner and Nataf,* 1986). There is an additional symmetry in surface wave observations: phase speeds with dip angles of θ and $\pi - \theta$ (with constant ϕ) are indistinguishable, as are observations at strike angles of ϕ and $\pi + \phi$ (with constant θ). This means that surface wave observations cannot

distinguish between the left-dipping foliation plane in **Figure 1a** from a right-dipping foliation plane that has been rotated about the z-axis by 180°.

Some terminology is needed to help distinguish between the properties of the anisotropic medium from observations of anisotropy with surface waves. By "inherent anisotropy", we mean the anisotropy of the untilted hexagonally symmetric elastic tensor given by the moduli A, C, N, L, and F. We summarize the inherent anisotropy of a hexagonally symmetric medium with the Thomsen parameters (*Thomsen*, 1986; *Helbig and Thomsen,* 2005; *Anderson and Thomsen*, 2015):

$$\varepsilon \equiv \frac{A-C}{2C} \approx \frac{V_{ph}-V_{pv}}{V_p} \tag{4}$$

$$\gamma \equiv \frac{N-L}{2L} \approx \frac{V_{sh}-V_{sv}}{V_s} \tag{5}$$

$$\delta \equiv \frac{(F+L)^2-(C-L)^2}{2C(C-L)} \approx \frac{F+2L-C}{C} \tag{6}$$

where ε is referred to as inherent "P-wave anisotropy" and γ is called inherent "S-wave anisotropy". A so-called "elliptical" anisotropic medium is one in which δ = ε, in which case P-wave and SH-wave fronts are elliptical and SV-wave fronts are spherical. As shown in the Appendix, upon tilting and reorienting in strike angle, a hexagonally symmetric elastic tensor can be decomposed into the sum of an azimuthally invariant (or effective transversely isotropic) tensor and an azimuthally anisotropic tensor. We refer to the moduli that compose the azimuthally invariant tensor ($\hat{A},\hat{C},\hat{N},\hat{L},\hat{F}$) as the "apparent" transversely isotropic moduli because these moduli govern the azimuthally averaged phase speeds of Rayleigh and Love waves. The Thomsen parameters can be recomputed using these moduli and they define apparent quasi-P wave and quasi-S wave radial anisotropy:

$\hat{\varepsilon} \equiv (\hat{A} - \hat{C})/2\hat{C}$, $\hat{\gamma} \equiv (\hat{N} - \hat{L})/2\hat{L}$. As discussed later, previous observational studies of radial anisotropy have estimated apparent radial anisotropy rather than the inherent anisotropy of the medium if earth media are, in fact, not oriented with a vertical symmetry axis.

A tilted hexagonally symmetric elastic tensor will generate both radial and azimuthal anisotropy in surface waves. **Figure 1b** demonstrates how apparent SV-wave azimuthal and apparent S-wave radial anisotropy (Rayleigh-Love discrepancy) vary as a function of dip angle. Note that only the dip angle is changing so that the inherent anisotropy is constant as apparent anisotropy changes. These curves are computed from a simple elastic tensor. For this model, the amplitude of azimuthal anisotropy increases with increasing dip angle (θ), and the apparent radial anisotropy decreases with increasing dip angle. When the dip angle is 0, there is strong positive apparent S-wave radial anisotropy but no azimuthal anisotropy. At some dip angle, the apparent radial anisotropy vanishes and the azimuthal anisotropy is non-zero. As the dip angle increases further, the apparent radial anisotropy becomes negative (meaning Vsv is greater than Vsh) and azimuthal anisotropy attains it maximum value. This example is intended to qualitatively illustrate the trend with dip angle; the details (e.g., the absolute amplitude, the crossing point, and the number of crossing points) depend on the elastic tensor itself (especially F or η).

The computation of Rayleigh and Love wave phase velocities from a given tilted hexagonally symmetric medium is discussed in the Appendix.

4. Model parameterization and constraints in the inversion

Our model parameterization, as well as the allowed variations in the model, are similar to

those described by *Shen et al*., (2013a, 2013b) in the inversion of isotropic Rayleigh wave phase speeds and receiver functions for an isotropic Vsv model of the crust and uppermost mantle in the western and central US. In fact, our model covers a subset of the region of Shen's model, which is the starting model for the inversion performed in this paper. Shen's model is isotropic with $V^0s = Vsh = Vsv$, $\eta^0 = 1$, and $V^0p = Vpv = Vph = 2.0*Vs$ in the sediments, $V^0p = Vpv = Vph = 1.75*Vs$ in the crystalline crust and mantle, density is computed through depth-dependent empirical relationships relative to Vs (*Christensen and Mooney*, 1995; *Brocher*, 2005), and the Q model is taken from the AK135 model (*Kennett et al*., 1995). Here, we fix the density and Q models to those values found by Shen.

In the crust and mantle we assume that the elasticity tensor possesses hexagonal symmetry with orientation given by the dip and strike angles (**Fig. 1a**). The depth dependence of the elastic moduli A, C, N, L, and F (or Vph, Vpv, Vsh, Vsv, and η) is represented by four B-splines in the crystalline crust from the base of the sediments to Moho, and five B-splines in the mantle from Moho to 200 km depth. Beneath 200 km the model is identical to AK135. The B-spline basis set imposes a vertical smoothing constraint on the model in both the crust and the mantle. If sedimentary thickness in Shen's model is less than 5 km, then the sediments are isotropic and are fixed to the model of Shen in which the depth dependence of Vs is represented by a linear function. Otherwise, as described below, S-wave anisotropy is introduced in the sediments by varying Vsh.

In addition to the parameterization, there are model constraints that govern the allowed variations around the starting model (V^0s, V^0p, η^0) in the inversion (described in the next section). Because we perform a Monte Carlo inversion, which involves only forward modeling, the imposition of the constraints is straightforward as they affect only the choice

of models that we compare with data; i.e., which models are used to compute the likelihood function. In the following, when referring to the seismic velocities $\left(V_{PV}=\sqrt{C/\rho}, V_{PH}=\sqrt{A/\rho}, V_{SV}=\sqrt{L/\rho}, V_{SH}=\sqrt{N/\rho}\right)$ and $\eta = F/(A-2L)$ we mean the inherent elements of a hexagonally symmetric elasticity tensor; that is, the inherent characteristics of the elasticity tensor prior to tilting. (1) Constancy of tilt angles in the crust and mantle. At each location, the dip and strike angles (tilt angles θ, ϕ) that define the orientation of the symmetry axis of anisotropy are constant through the crystalline crust and constant through the mantle, although the crustal and mantle angles are allowed to differ from each other. (2) Range of model variables. The allowed variations of the elastic parameters in the crystalline crust and mantle relative to the starting model are as follows: Vsv±0.05*V^0s, Vsh±0.15*V^0s, Vpv±0.15*V^0p, Vph±0.15*V^0p. In addition, in the crust $\eta_{crust} \in [0.6,1.1]$ and in the mantle it lies in the smaller range $\eta_{mantle} \in [0.85,1.1]$. Also, the tilt angles range through the following intervals: $\theta \in [0,90°]$, $\phi \in [0,180°]$. (3) Sedimentary model. If sedimentary thickness is less than 5 km in Shen's model, the sedimentary part of the model remains unchanged (i.e., it is isotropic and identical to Shen's model). If the thickness is greater than 5 km, then only the Vsh part of the model is perturbed to introduce S-wave radial anisotropy with $\gamma \in [0,0.2]$; i.e., a maximum S-wave anisotropy of 20%. No tilt is introduced to the elastic tensor in the sediments. (4) Vp/Vs ratio. Vp/Vs = (Vpv+Vph)/(Vsv+Vsh) $\in$ [1.65,1.85]. (5) Monotonicity constraint. Vsv, Vsh, Vpv, and Vph each increase monotonically with depth in the crystalline crust. A monotonicity constraint is not imposed on η or on any of the variables in the mantle. (6) Positive anisotropy. Vsh > Vsv, Vph > Vpv. (7) Fixed points of the model. Density and crustal thickness are not changed relative to the starting model.

The constraints can be considered to fall into two groups, one group is based on prior knowledge, and the other is introduced to simplify the model. The Vp/Vs ratio, positive anisotropy, and the fixed points of the model constraints are based on prior knowledge. For example, the inherent anisotropies are set to be positive because crustal rock samples show slow velocity perpendicular to the foliation plane and fast velocity within the foliation plane, and anisotropy caused by layering also shows positive inherent anisotropy (*Anderson and Thomsen,* 2014; *Tatham et al.*, 2008; *Brownlee et al.*, 2011; *Erdman et al.*, 2013). We set the sedimentary thickness and crystalline crustal thickness constant based on the receiver function observations by *Shen et al*. (2013b). The Vp/Vs ratio is constrained to be within 1.65 to 1.85 because most other observations of Vp/Vs fall in this range (e.g., *Lowry and Perez-Gussinye,* 2011; *Christensen*, 1996; *Buehler and Shearer*, 2014).

In constrast, constraints such as the vertically constant tilt angle in the crust and mantle and monotonic increase of seismic wave speeds in the crust are used to simplify the resulting models. Everything else being equal, we prefer simpler models because they are more testable and falsifiable. For example, we could have parameterized the tilt angles as depth-varying and still fit our data. (In fact, there are always an infinite number of possible and more complex alternatives that include more ad hoc hypotheses.) Without prior knowledge, more complex models can hardly be proven wrong because they can always fit the data. Besides, little can be learned from such complexities because they are not derived from the data. On the other hand, a simple model cannot always fit the data (e.g., a constant velocity profile cannot fit the dispersion curves), so it is more easy to prove wrong (if it is). When a model is too simple to fit the data, we then add complexity to the model or loosen constraints. Because this kind of added complexity is motivated by the data, it is more likely

to provide information about the earth. Therefore, we view the vertically constant tilt angle and monotonicity constraints as hypotheses that we test empirically. If we are unable to fit aspects of the data acceptably, we will return and loosen these constraints to help fit the data. Otherwise, these constraints are kept to generate a simple model.

In summary, we seek an anisotropic model that is relatively close to the isotropic model of Shen, possesses hexagonally symmetric anisotropy with a symmetry axis of locally constant but geographically variable orientation in the crystalline crust and upper mantle, has only positive P-wave and S-wave anisotropy, a Vp/Vs ratio that varies around that of a Poisson solid, and possesses seismic velocities that increase with depth in the crust. Given the allowed variations in the elastic moduli, the maximum S-wave anisotropy (γ) considered in both the crust and mantle is 20%. Because Shen's model was constructed with Rayleigh waves (and receiver functions) it only weakly constrains Vp and Vsh, but has rather strong constraints on the sedimentary and crustal thicknesses and Vsv in the crust. For this reason, we allow in our inversion wider variation in Vp and Vsh than in Vsv. η is allowed to vary through a wider range in the crust than mantle based on measurements of elastic tensors for crustal rocks (*Tatham et al., 2008; Brownlee et al*., 2011; *Erdman et al*., 2013) and olivine (*Babuška*, 1991), which is believed to be the major contributor to mantle anisotropy, and also to be consistent with mantle elastic moduli in other studies (e.g., *Montagner and Anderson,* 1989). We do not allow sedimentary thickness or crustal thickness to vary at all because receiver functions are not used in our inversion. However, we find that in areas where the sediments are thicker than 5 km, radial anisotropy is needed in order to fit the data at short periods. In this case, we introduce only S-wave anisotropy in the sediments (no P-wave anisotropy, no deviation of η from unity), which is probably physically unrealistic,

so we do not interpret the resulting model of anisotropy in the sediments. However, regions where sediments are thicker than 5 km in Shen's model are relatively rare in the western US.

5. Bayesian Monte Carlo inversion

The data that are inverted are similar to those shown in **Figure 6** for two locations in the western US. We apply a Bayesian Monte Carlo method to invert the data at each location. The implementation of the inversion is very similar to the method described in detail by *Shen et al*. (2013a), but we do not apply receiver functions. We construct observations such as those in **Figure 6** on a 0.2°x0.2° grid. The isotropic model constructed by *Shen et al*. (2013b), which is our starting model, is constructed on the irregular grid given by the station locations where the receiver functions are defined. In contrast, we construct our model on a regular 1°x1° grid across the central and western US. At each grid point, the starting model in our inversion is Shen's model at the nearest station, which in some cases may be as much as 40 km away.

At each location the prior probability distribution is defined relative to Shen's model based on the constraints described in the previous section. The prior distribution guides the sampling of model space. A model is determined to be acceptable or not based on its likelihood function *L(m)*, which is related to the chi-squared misfit *S(m)* (*Shen et al*., 2013a; *Xie et al*., 2013). *L(m)* and *S(m)* are defined as follows:

$$L(m) = \exp(-\frac{1}{2}S(m)) \quad (7)$$

where

$$S = \sum_i \frac{(D(m)_i^{predicted} - D_i^{observed})^2}{\sigma_i^2} \quad (8)$$

The chi-squared misfit *S(m)* measures the weighted difference between the observed and predicted dispersion curves, where the forward model is computed as described in the Appendix. The chi-squared misfit is composed of four terms, corresponding to the four curves at each location shown in **Figure 6**. The first two are for isotropic Rayleigh and Love waves. The other two are for the amplitude and fast-axis direction of Rayleigh wave azimuthal anisotropy. The only weights in the misfit function are the standard deviations of the measurements.

The model sampling process and acceptance criteria follow the procedure described *Xie et al*. (2013) where the partial derivatives are updated when 200 more models are accepted. Because the model sampling will not complete until at least 5000 models are initially accepted, the partial derivatives are updated at least 25 times during the sampling. After the sampling is complete, the entire set of initially accepted models is put through the selection process again to remove models with larger misfit (*Xie et al*., 2013). On average, models are accepted up to about twice the rms misfit of the best-fitting model. This reselected model set composes the (truncated) posterior probability distribution**,** which is the principal output of the inversion. The posterior distribution satisfies the constraints and observations within tolerances that depend on data uncertainties.

Examples of prior and posterior probability distributions for the inherent variables at 20 km depth are shown in **Figures 7 and 8** for the same two locations for which we present the data in **Figure 6**. The prior distributions are strongly shaped by the model constraints. For example, Vsv displays a narrower prior distribution because only 5% perturbations relative

to the starting model are sampled compared to 15% perturbations in Vsh, Vpv, and Vph. The non-uniform shape of many of the distributions arises from constraints that tie model variables between different depths or of different types, such as the monotonicity constraint. The prior distributions for the dip and strike angles are uniform, however, because they are constant across the crust and, therefore, are not explicitly tied to choices of variables at different depths or of different types. The posterior distribution is wider for variables that are poorly constrained by the data (e.g., Vph, η) than for those that are well constrained (e.g., θ, ϕ, Vsv, Vsh). Note that the crustal dip and strike angles, θ and ϕ, are well constrained by the data in that their posterior distributions are relatively narrow. However, the posterior distribution of the crustal strike angle is bimodal, defining two model groups in which strike angles differ by 90°, on average. These two groups of models are presented as blue and red histograms in **Figures 7 and 8**. The physical cause of this bifurcation is discussed in **Section 6.2** below.

We define "Group 1" (red histograms) to be the set of models with a crustal strike angle that approximately parallels the Rayleigh wave fast direction averaged between 10 sec and 22 sec period. "Group 2" is the set of models with a strike angle that is approximately orthogonal to the Rayleigh wave fast axis direction in this period range. There are subtle differences between the crustal moduli A, C, N, and L between the two groups, but much stronger differences in η, dip angle θ, and the non-elliptical parameter (ε-δ). Typically, Group 1 has larger values of η and more nearly elliptical anisotropy ($\varepsilon \approx \delta$) in the crust, whereas Group 2 has smaller η and a more non-elliptical anisotropy. Also, Group 1 models tend to have a slightly larger crustal dip angle, on average. We believe that the bifurcation in model space is controlled fundamentally by η, which is poorly constrained in the prior

distribution or by the data. The effect of the bifurcation on our conclusions also will be discussed further in the next section of the paper.

Ultimately, we summarize each posterior distribution by its mean and standard deviation, which define the final model and uncertainty at each depth, and for each model variable. **Table 1** presents these statistics for the posterior distributions shown in **Figures 7 and 8**. **Figure 9** presents vertical profiles of Vsv and Vsh (related to the moduli L and N), showing the mean and standard deviation for Group 1 and Group 2 models separately at locations A and B in the Basin and Range and Colorado Plateau (**Fig. 3a**), respectively. Differences between the moduli of the two groups are discussed further below. These profiles are derived to fit the data presented in **Figure 6**, where we also show how well the data are fit by the mean model from each group (Group 1: solid lines, Group 2: dashed lines). The two groups fit the isotropic phase speed data nearly identically but do display small differences in the details of the fit to Rayleigh wave azimuthal anisotropy, although both fit within data uncertainties. The differences in fit are largest for the amplitude of azimuthal anisotropy above 30 sec period where uncertainties in this variable grow. Note that both groups fit the fast azimuth direction of Rayleigh wave azimuthal anisotropy equally well, even though the strikes angles of the crustal anisotropy differ by 90°.

In addition, posterior covariances between different model variables at a particular depth, and a given model variable at different depths, can also be determined from the posterior distributions. In fact, we compute posterior correlation matrices in which the elements of the covariance matrix are normalized by the appropriate standard deviation, which normalizes the diagonal elements of the matrix to unity. In practice, we use the terms correlation and covariance interchangeably here.

As an example, the posterior covariance matrix for five variables ($\gamma,\varepsilon,\delta,\theta,\phi$) at 20 km depth is presented in **Figure 10** for a point in the Basin and Range province (point A in **Fig. 3a**). Most correlations are relatively weak, γ is negatively correlated with ε and δ, ε and δ are strongly positively correlated in order to keep a relatively constant $\varepsilon-\delta$. Importantly, θ has no correlation with other variables except δ. A correlation between these two variables is probably not surprising because δ affects the speed of waves propagating at an angle through the medium (oblique to the symmetry axis) and θ orients the medium.

Similarly, **Figure 10b-d** shows the posterior covariance matrix for each model variable with the same model variable at different depths. This is again for point A in the Basin and Range province, where crustal thickness is about 31 km. Thus, depths greater than 31 km are in the mantle and shallower depths are in the crust. Most of the correlations in this case are positive. The correlation length (a measure of the rate of decay of the covariance with distance) in the crust is smaller than in the mantle because the vertical resolution is better. The B-splines in the crust only span from the bottom of the sediments to the Moho (less than 30 km here), whereas in the mantle they span about 170 km. The correlation length for γ is smaller than ε and δ, indicating a better vertical resolution of γ.

Covariance matrices such as the examples presented here illuminate the implications of the parameterization and constraints imposed in the inversion, but we only interpret this information qualitatively; it is not used formally.

6. Results

Love wave phase speed dispersion curves extend only up to 50 sec period and the Rayleigh

wave anisotropic dispersion curves also do not extend to very long periods. Thus, constraints on crustal structure are stronger than on the mantle. We have tested variations in mantle parameterizations and constraints, and found that changes affect estimated crustal structure within uncertainties. In the following, therefore, we will concentrate detailed discussion on the crustal part of our model, and will discuss mantle structure principally in a spatially averaged sense. Later work will specifically aim to improve and interpret the mantle model in a spatially resolved sense.

6.1 Crustal anisotropy across the western US

The results presented to this point are only for two locations, in the Basin and Range province and the Colorado Plateau (points A and B, **Fig. 3a**). We have applied the Bayesian Monte Carlo inversion described above to the US west of 100°W longitude and produced a 3D model of the crustal elastic tensor (with uncertainties) on a 1°x1° grid across the region. The mean and standard deviation of aspects of the posterior distribution averaged across the crystalline crust (from the base of the sediments to Moho) are shown in **Figures 11** and **12**.

As discussed above, the posterior distribution bifurcates at each location into two disjoint groups of models based on the strike angle, and we present results in the crust for both groups of models. For Group 1, crustal anisotropy is nearly elliptical meaning that the Thomsen parameters ε and δ, defined in **Equations (4) and (6)**, are nearly identical. **Figure 11a** shows that ε – δ is close to zero across the entire western US for Group 1 models. We refer to ε – δ as the "non-elliptical" parameter because values much larger or smaller than zero indicate the deviation from elliptical anisotropy. Group 2 models have more non-elliptical anisotropy as **Figure 11d** illustrates, and ε is generally greater than δ so that the non-elliptical parameter is generally positive.

Although the elasticity tensors in the two groups of models differ in the extent to which the anisotropy is non-elliptical, the geographical distribution and the amplitude of inherent S-wave anisotropy, given by the Thomsen parameter γ (**Equation (5)**), are similar. The amplitude averages about 3.9% for Group 1 and 4.2% for Group 2 (**Fig. 11b,e**). The differences in γ between Groups 1 and 2 are within estimated uncertainties (**Fig. 12a,d**), which average about 2% across the region. On average, γ does not vary strongly with depth in the crust, as **Figure 13** illustrates. The error bars represent the inherent S-wave anisotropy at normalized crustal depth averaged across the study region. γ tends to be somewhat stronger in the shallow (~4%± 2%) and deep (~6%± 3%) crust than in the middle crust (~3%± 2%), but the trend is weak and does not occur everywhere. The amplitude of inherent S-wave anisotropy is everywhere positive (as it is constrained to be), and is fairly homogeneous laterally across the western US. It is, however, largest in the Basin and Range province and smallest in the Colorado Plateau and the western Great Plains. The positivity constraint on γ does not have to be relaxed anywhere to fit the data. γ is larger than its uncertainty across nearly the entire western US with the possible exception of some of the peripheral regions where uncertainties grow due to less ideal data coverage. For this reason, we suggest that γ not be interpreted near the Pacific coast.

Compared with earlier estimates of (apparent) S-wave radial anisotropy across the western US (e.g., *Moschetti et al*., 2010a, 2010b), the amplitude of γ (inherent S-wave anisotropy) does not change as strongly across the region. This discrepancy is correlated with the difference between 'inherent' and 'apparent' anisotropy, and is discussed below in **Section 6.5**.

In contrast with γ, the dip angle does change appreciably across the study region and the dip

and strike angles differ appreciably between the two model groups. Differences between dip angles, shown by varying the background coloration in **Figure 11c,f**, are somewhat subtle. The spatially averaged uncertainty in the dip angle across the western US is 9° to 10° for both model groups. The geographical distribution of the variation in dip angle is similar between the two groups of models, but models in Group 2 have dip angles that average about 25° whereas Group 1 models average about 30°. Recall that the dip angle in the elasticity tensor is introduced to produce azimuthal anisotropy. Thus, elasticity tensors with nearly elliptical anisotropy must be tilted more to fit the azimuthal anisotropy data than tensors with substantially non-elliptical anisotropy. The dip angle in the crust everywhere across the western US is less than about 70° and greater than about 10°, with the majority of the angles falling within the range of 10º and 45º. The Basin and Range province has a shallower dip whereas the Colorado Plateau has a steeper dip, on average.

There is a more prominent difference in strike angle than dip angle between the two groups of models. The strike angle directions for Group 1 and Group 2 models differ by 90°. This is a significant enough observation to warrant its own subsection, and is discussed further in **Sections 6.2 and 6.3**. Uncertainty in strike angle averages 12°-13° across the study region.

There are also significant differences between the two groups of models in η and the other Thomsen parameters, ε (inherent P-wave anisotropy) and δ. η averages about 0.83 ($\pm$0.08) for Group 1 models and 0.077 ($\pm$0.07) for Group 2. In addition, there are larger values of inherent P-wave anisotropy (ε) in Group 1 (8.1%$\pm$4.8%) than in Group 2 (6.6%$\pm$4.2%). Group 1 models have nearly elliptical anisotropy, so $\delta \approx \varepsilon$. Thus, for Group 1 models, δ is on average larger (8.5% $\pm$ 6.7%) than for Group 2 models (2.8% $\pm$ 5.3%). For Group 2 models $\delta \ll \varepsilon$, on average.

6.2 On the cause of the bifurcation in strike angle of crustal anisotropy

The fact that two groups of solutions with orthogonal strike angles both fit the crustal sensitive Rayleigh wave data may be explained in terms of the phase speed surface produced by different elastic tensors. The phase speed surface can be computed by solving the Christoffel equation. For waves traveling in any direction, there are always three mutually orthogonal wave solutions, one (quasi-) P wave and two (quasi-) S waves. Normally, the S wave with faster speed is called S_1, and the slower one is called S_2. Note that S_1 and S_2 should not be associated with SV or SH waves, because S_1 and S_2 are defined based on the wave speed instead of the polarization direction.

Figure 14 shows the phase speed surface of P, S_1, and S_2 waves, together with the polarization direction of the S wave for two tilted elastic tensors with hexagonal symmetry, one is elliptical with a dip angle of 20° and strike angle of 210°, the other is non-elliptical with dip angle 20° and a strike angle 300°. Each surface plots a particular speed (Vs_1, Vs_2, P) for waves propagating in different directions. **Figure 14** shows a lower hemisphere plot so that horizontally propagating waves (surface waves) are sensitive to wave speeds at the edge of the diagram. These two tensors represent our Group 1 and Group 2 models that have different ellipticity properties and orthogonal strike angles. The most prominent feature of the non-elliptical tensor is that the polarization direction of the S_1 wave suddenly changes from radial to tangential at some degree oblique to the symmetry axis. A Rayleigh wave that is propagating horizontally in a hexagonally symmetric medium with a shallow to moderate dip is mainly sensitive to the phase speed of the S_2 wave (Vs_2). In the following paragraphs, therefore, we will concentrate discussion on the speed Vs_2. We will show that the two groups of elasticity tensors produce the same azimuthal pattern in wave speed Vs_2 even

though their strikes angles differ by 90°.

In an elliptical hexagonal medium (Group 1), the Vs_2 surface has its minimum value oblique to the symmetry axis. In a non-elliptical hexagonal material, the pattern of the Vs_2 surface is reversed: Vs_2 has its maximum value oblique to the symmetry axis. Because horizontally propagating Rayleigh waves are only sampling the outer margin of the wave speed surface, we plot the value of Vs_2 at the edge of the surface as a function of azimuth (**Fig. 15a**). We find that despite the orthogonal strike directions, the two groups of models produce similar azimuthal patterns of Vs_2, with the same fast axis directions. Group 1 models have their Vs_2 fast axis direction parallel to the strike angle of the elasticity tensor, whereas Group 2 models have their fast axis directions orthogonal to the strike. This phenomenon results in the same fast direction for the Rayleigh waves, even when the orientation of the inherent elasticity tensor is different.

In contrast with the propagation of S_2 waves, however, a horizontally propagating P wave is always fastest parallel to the strike of a dipping hexagonally symmetric elastic tensor (**Fig. 15b**). Therefore, a P wave's fast direction always indicates the strike direction.

In conclusion, for both groups of models the Rayleigh wave fast axis direction is the same even if the strike of the anisotropy rotates by 90°. However, the P wave fast directions in the two groups will be orthogonal to each other, consistent with a 90° rotation of the strike. Therefore, observations of P wave anisotropy provide unambiguous information about the orientation of the strike angle of anisotropy, but Rayleigh waves do not.

6.3 The strike angle of crustal anisotropy and the Rayleigh wave fast axis direction

As discussed in **Section 5**, the posterior distribution divides into two disjoint groups of

crustal models according to the estimated strike angle (ϕ) of anisotropy, which is defined in **Figure 1a**. The physical cause of this bifurcation is discussed in **Section 6.2**. Thus, at each spatial grid point there are two distinct distributions of elastic tensors and orientations (or tilts) that will fit the Rayleigh wave data approximately equally well. For Group 1, the set of models with approximately elliptical anisotropy ($\varepsilon \approx \delta$) and typically larger value of η, the distribution of strike angles is shown in **Figure 11c**. These strike angles are very similar to the Rayleigh wave fast axis directions for waves that sample the crust (e.g., 10-20 sec period, **Fig 4a**). **Figure 16** illustrates this fact by comparing the strike angles with the 16 sec period Rayleigh wave fast axis directions using blue symbols. The mean and standard deviation of the difference are 0.2° and 21.0°, respectively. The geographical distribution of the strike angles (and fast axis directions for crustal sensitive Rayleigh waves) are similar to those found by *Lin et al*. (2011), who discuss the geological coherence of the observations, so we forgo this discussion here.

The second group of models, Group 2, possesses strike angles that are distinct from Group 1, ε is typically significantly larger than δ, so the anisotropy is decidedly non-elliptical, and η is usually smaller than 0.8. As **Figure 16** also shows with red symbols, the strike angles of Group 2 are, on average, perpendicular to the strike angles of Group 1 such that the average angular difference and standard deviation are 90.2° and 8.8°, respectively. This distribution is tighter than the comparison with Rayleigh wave fast axis directions because Rayleigh wave fast axes at a particular period are measurements and are, therefore, noisy.

In summary, Rayleigh wave fast axis directions are ambiguously related to the strike of inherent crustal anisotropy. In fact, the fast axis direction will only parallel the strike direction if the crustal anisotropy is largely elliptical in nature. As information has grown on

the petrology of seismic anisotropy in the crust, evidence has mounted that crustal anisotropy is probably not strongly elliptical (e.g., *Tatham et al., 2008; Brownlee et al.*, 2011; *Erdman et al.,* 2013). Thus, the geologically favored models are probably from Group 2. Therefore, crustal sensitive Rayleigh waves must only be used with caution to reveal the orientation of the geological features that are causing the anisotropy. It is probably more likely for the fast axis direction of crustal sensitive Rayleigh waves to point perpendicular to the strike direction than parallel to it. Similarly, assuming nearly-vertical shear waves, crustal shear wave splitting will have its fast axis in the direction of the Rayleigh-wave fast axis. Therefore, the fast splitting direction of crustal SKS is also more likely to point perpendicular to the strike direction than parallel to it.

To recover unambiguous information on the strike angle, other types of data need to be introduced. As discussed in **Section 6.2**, observations of crustal P wave anisotropy can resolve the ambiguity because the P wave fast direction is always parallel to the strike direction. Admittedly, however, this is a difficult observation to make.

6.4 On the interpretation of the inferred dip angle

There are two alternative interpretations of the inferred dip angle, θ: that it is a measurement of the actual geometry of the foliation plane of material composing the medium, or that it is a proxy for another potentially unknown non-geometric variable. We will first discuss the latter alternative.

First, it is possible that the observed dip angle is proxy for other variables. Even though our models are expressed in terms of a tilted hexagonally symmetric medium, crustal anisotropy may not actually be hexagonally symmetric, or the approximation to hexagonal symmetry may not be accurate everywhere. Crustal anisotropy may indeed possess lower order

symmetry than hexagonal. Tilting a material can have the effect of decreasing the apparent symmetry of the material if viewed in the same coordinate system (*Okaya and McEvilly*, 2003). In principle, therefore, a lower order elasticity tensor could be approximated by a higher order tensor (e.g., hexagonally symmetric) through tilting. It is possible that the efficacy of this approximation is enhanced by the fact that surface wave travel time data are insensitive to 8 of the 21 moduli that constitute a general elasticity tensor (Appendix). It is conceivable, therefore, that the effect on our data that we interpret as a tilt (non-zero dip angle) could have resulted from the non-hexagonal component of the actual elasticity tensor of the medium. What we would estimate in this case is an "apparent dip angle" that is proxy for the extent to which the medium deviates from hexagonal symmetry.

We have experimented with numerically fitting tilted hexagonally symmetric elasticity tensors to nearly orthorhombic tensors from crustal rock samples (*Tatham et al., 2008; Brownlee et al*., 2011; *Erdman et al*., 2013) using only the 11 combinations to which observations of the 2ψ component of Rayleigh wave and the azimuthally isotropic Rayleigh and Love wave data are sensitive (Appendix). We estimate an apparent dip angle that measures the medium's deviation from hexagonal symmetry. Apparent dip angles resulting from this fit typically range between 15˚ to 25˚. The dip angles that we infer, therefore, may be a result of approximating orthorhombic or other lower-symmetry material with hexagonally symmetric tensors, in which case steeper dip angles would reflect a greater deviation from hexagonal symmetry.

Second, there is also likely to be at least some component of the inferred crustal elasticity tensors related to the actual dip of the foliation of the material. In fact, variations in observed dip angles make geologic sense in some regions. For example, observed dips are

shallow beneath the Basin and Range province, which is consistent with large-scale crustal extension along low-angle normal faults and horizontal detachment faults (e.g. *Xiao et al*. 1991; *Johnson and Loy*, 1992; *John and Foster*, 1993; *Malavieille* 1993). The steeper dip angles observed in California are also consistent with a lower crust consisting of foliated Pelona-Orocopia-Rand schist (e.g. *Jacobson* 1983; *Jacobson et al*. 2007; *Chapman et al*. 2010), which was under-plated during Laramide flat-slab subduction (e.g. *Jacobson et al*., 2007). In other regions, such as beneath the Colorado Plateau, the potential geologic meaning of the steeper observed dip angles is less clear; perhaps the steeper dips are an indication of a change in crustal composition resulting in an elastic tensor with low symmetry.

6.5 Comparison with previous studies: Inherent versus apparent anisotropy

A tilted hexagonally symmetric elastic tensor will generate both apparent radial and azimuthal anisotropy in surface waves as demonstrated by **Figure 1b**. At a given depth, referencing the notation in the Appendix, we define apparent S-wave radial anisotropy as:

$$\hat{\gamma} = (\hat{N} - \hat{L}) / 2\hat{L} \tag{9}$$

where

$$\hat{N} = (C_{11} + C_{22}) / 8 - C_{12} / 4 + C_{66} / 2 \qquad \hat{L} = (C_{44} + C_{55}) / 2 \tag{10}$$

We also define the amplitude of apparent SV-wave azimuthal anisotropy as:

$$|G| / L = \sqrt{G_c^2 + G_s^2} \Big/ L \tag{11}$$

where

$$G_c = (\delta C_{55} - \delta C_{44})/2 = (C_{55} - C_{44})/2 \quad (12)$$

$$G_s = \delta C_{45} = C_{45} \quad (13)$$

The components of the modulus matrix, $C_{\alpha\beta}$, are functions of the inherent elastic moduli (A,C,N,L,F) and tilt (θ,ϕ). The strength of inherent S-wave anisotropy is defined by equation (5).

As shown in **Figure 1b**, when the inherent elastic moduli (A,C,N,L,F) are fixed, variations in dip angle θ produce the variations in the apparent anisotropies. The amplitudes of apparent anisotropies are always smaller than the inherent anisotropy except for two extreme cases, $\theta = 0°$ and $\theta = 90°$. Thus, if earth structure has $\theta \in (0°,90°)$, then neither apparent radial nor apparent azimuthal anisotropy will reflect the real strength of anisotropy (inherent anisotropy) in the earth.

In studies that use either isotropic dispersion curves or azimuthally anisotropic dispersion curves alone, it is the apparent anisotropy instead of the inherent anisotropy that is estimated. For example, in studies of radial anisotropy using surface waves (e.g., *Moschetti et al*., 2010a, 2010b; *Xie et al*., 2013), only the azimuthally isotropic Rayleigh and Love wave dispersion curves are used to produce a transversely isotropic model (hexagonally symmetric with a vertical symmetry axis), which produces no azimuthal anisotropy. Because the azimuthally isotropic dispersion curves are only sensitive to the effective transversely isotropic part of the elastic tensor ($\hat{A},\hat{C},\hat{N},\hat{L},\hat{F}$, Appendix), this transversely isotropic model is the effective transversely isotropic (ETI) part of our model. To prove this, we compute the ETI part of our model, from which the apparent S-wave radial anisotropy can be generated (**Fig. 17**). The apparent S-wave radial anisotropy for both Group 1 and

Group 2 models are very similar to each other, they both change appreciably across the study region, with large amplitudes in the Basin and Range province and small amplitudes in the Colorado Plateau. This pattern is very similar to that observed by *Moschetti et al*. (2010b), and thus demonstrates that inversion with isotropic dispersion curves alone results in observations of apparent S-wave radial anisotropy. Similarly, inversion with azimuthally anisotropic dispersion curves alone results in apparent SV-wave azimuthal anisotropy (e.g., *Lin et al*., 2010).

The apparent radial and apparent azimuthal anisotropy reflect different aspects of the inherent elastic tensor and both mix information from the inherent elastic moduli and the orientation. As described in **Section 6.1**, the amplitude of γ, the inherent S-wave anisotropy, does not change strongly across the region, and averages about 4%. In contrast, the amplitude of $\hat{\gamma}$, the apparent radial anisotropy, changes strongly across the region in a pattern similar to the variation of the dip angle θ, and averages to about 2%. Thus, the lateral variation of $\hat{\gamma}$ results mainly from the variation of θ, and does reflect the strength of γ.

In most surface wave studies, only the apparent anisotropies are estimated. Therefore, the results depend on the unknown orientation of the medium, which limits their usefulness to constrain the elastic properties of the medium (e.g., the inherent S-wave anisotropy, γ).

6.6 Mantle anisotropy across the western US

Although the focus of this paper is on crustal anisotropy we present here a brief discussion of the mantle anisotropy that emerges from the inversion. **Figure 18** shows the prior and

posterior distributions at 60 km depth at point A in the Basin and Range province. At this point, the mean of the posterior distribution is between 4-5% for both inherent S-wave (γ) and P-wave (ε) anisotropy, both the dip and strike angles are fairly well resolved with a mean dip angle of 27° (±7°) and strike angle of 66° (±8°), the mean of the posterior distribution for η is 0.96 (±0.04) which is much higher than in the crust, and the anisotropy is indistinguishable from elliptical (ε-δ = -0.04 ± 0.06). The nearly elliptical nature of mantle anisotropy is also quite different from what we observe in the crust. This location is fairly typical of mantle anisotropy across the western US, as γ averages 4.4% (±2.6%) across the western US with an average dip angle of 21° (±8°). We note in passing that such a steep dip angle may result from a strong orthorhombic component to the mantle elasticity tensors and may not result from the actual tilt of the medium. Because, unlike the crust, the posterior distribution in the mantle does not bifurcate according to strike angle, Rayleigh wave fast axis directions are unambiguously related to the strike angle in the mantle. Because mantle anisotropy is nearly elliptical (with η close to one), Rayleigh wave fast axes actually align with the strike angle rather than orthogonal to it. However, mantle strike angle is not everywhere well determined across the region as the average uncertainty is nearly 30°. The inability to resolve mantle strike angle unambiguously across the region with the current data set and method is one of the reasons we focus interpretation on crustal anisotropy here and will return to mantle anisotropy in a later contribution.

7. Summary and Conclusions

The motivation of this paper is to present a method of inversion that reconciles observations of radial and azimuthal anisotropy with surface waves. Studies of radial (or polarization)

anisotropy and azimuthal anisotropy tend to interpret such observations by invoking elasticity tensors with hexagonal symmetry, due to their simplicity but also because earth (particularly crustal) materials often display approximate hexagonal symmetry. Hexagonal symmetry with a vertical symmetry axis is transversely isotropic, so no azimuthal anisotropy exists under this assumption. Therefore, whether explicitly or implicitly, studies of radial anisotropy typically assume a vertical symmetry axis and studies of azimuthal anisotropy suppose a horizontal symmetry axis. Because observations of radial and azimuthal anisotropy often coincide spatially, the common assumptions of the orientation of symmetry axes are inconsistent. The method we present here is also based on the assumption of a hexagonally symmetric elasticity tensor, but with an arbitrarily oriented symmetry axis, which we refer to as "tilted". The elasticity tensor itself at each depth is given by five elastic moduli (A, C, N, L, and F or η) and the tilt is defined by two rotation angles: the dip and strike, which are illustrated in **Figure 1a**. We refer to these moduli as "inherent", as they reflect the characteristics of the elasticity tensor irrespective of its orientation.

We show that observations of radial anisotropy and the 2ψ component of azimuthal anisotropy for Rayleigh waves obtained using USArray in the western US can be fit well by tilted hexagonally symmetric elastic tensors in the crust and mantle, subject to the constraints listed in the text. The inversion that we produce is a Bayesian Monte Carlo method, which yields a posterior distribution that reflects both the data and prior constraints. The most noteworthy constraint is that the tile angles (dip, strike) are constant in the crust and mantle, but may differ between the crust and mantle. The results are summarized as posterior distributions of smoothly depth-varying inherent (unrotated) moduli (A or Vph, C

or Vpv, N or Vsh, L or Vsv, and F or η) as well as dip and strike angles. The standard deviation of the posterior distribution defines the uncertainties in these quantities. Anisotropy is summarized with the Thomsen parameters, inherent S-wave anisotropy (γ) and inherent P-wave anisotropy (ε), and either η or δ (which is the third Thomsen parameter).

Because the crust is constrained by the data better than the mantle, and γ (inherent S-wave anisotropy) is determined more tightly than ε (inherent P-wave anisotropy), we focus interpretation on γ in the crust as well as the tilt angles. Major results include the following. (1) γ is fairly homogeneous vertically across the crust, on average, and spatially across the western US. (2) Averaging over the region of study and in depth, γ in the crust is approximately 4%±2%. (3) Crustal strike angles (ϕ) in the posterior distributions bifurcate into two sets of models that we refer to as Groups 1 and 2. Models in Group 1 have strike angles that approximately parallel crust-sensitive Rayleigh wave fast axis directions, and typically have larger values of η and nearly elliptical anisotropy ($\varepsilon \approx \delta$). Group 2 models have strike angles that are approximately orthogonal to crust-sensitive Rayleigh wave fast directions, smaller values of η, and more strongly non-elliptical anisotropy where typically $\varepsilon > \delta$. Mantle strike angles do not bifurcate as they do in the crust because of tighter constraints imposed on η in the inversion. (4) γ in the crust is approximately the same in the two groups of models. (5) Dip angles in the two groups of models vary spatially in similar ways and display geological coherence; for example, they are smaller in the Basin and Range province than in the Colorado Plateau or the Great Plains. However, in Group 1 they are slightly larger than in Group 2, averaging 30°±10° in Group 1 and 25°±9° in Group 2. (6) Rayleigh wave fast axis directions are ambiguously related to the strike of anisotropy,

but recent studies of the anisotropy of crustal rocks (e.g., *Tatham et al., 2008; Brownlee et al.*, 2011; *Erdman et al.,* 2013) imply that the crustal anisotropy is probably not nearly elliptical, which favors Group 2 models. Therefore, under the assumption that crustal anisotropy is approximately hexagonally symmetric with an arbitrary tilt, Rayleigh wave fast axis directions for crust sensitive Rayleigh waves will be oriented orthogonal rather than parallel to the strike of anisotropy. Interpretation of Rayleigh wave fast axis directions in terms of crustal structure must be performed with caution. (7) The estimated dip angle may be interpreted in two alternative ways. It is either an actual measurement of the dip of the foliation plane of anisotropic material within the crust, or it is proxy for another non-geometric variable, most likely a measure of the deviation from hexagonal symmetry of the medium. (8) By attempting to estimate the inherent moduli that compose the elastic tensor of the crust (and mantle), our approach differs from earlier studies that produce measurements of "apparent" moduli. Because tilting a medium produces apparent radial and apparent azimuthal anisotropies that are both smaller than the inherent anisotropy in amplitude, previous studies have tended to underestimate the strength of anisotropy.

In the future, we intend to improve long period data in order to produce improved results for the mantle and apply the method more generally to observations of surface wave anisotropy. It will also be desirable to apply increasingly strong constraints on allowed anisotropy and continue to revise the interpretation of results as more information accrues about crustal anisotropy from laboratory measurements. In particular, it may make sense to experiment with more general theoretical models of anisotropy in the inversion, perhaps by considering a mixture of elasticity tensors with hexagonal and orthorhombic symmetry. Ultimately, we aim to interpret the results in terms of petrological models that agree with the inferred

elasticity tensor.

Acknowledgments. The authors are grateful to Don Anderson, Peter Molnar, Jean-Paul Montagner, and David Okaya for helping to inspire this work and for conversations that improved it. They also thank Craig Jones and Vera Schulte-Pelkum for comments on an early draft of this paper. The facilities of the IRIS Data Management System, and specifically the IRIS Data Management Center, were used to access the waveform and metadata required in this study. The IRIS DMS is funded through the National Science Foundation and specifically the GEO Directorate through the Instrumentation and Facilities Program of the National Science Foundation under Cooperative Agreement EAR-0552316. This work utilized the Janus supercomputer, which is supported by the National Science Foundation (award number CNS-0821794) and the University of Colorado Boulder. The Janus supercomputer is a joint effort of the University of Colorado Boulder, the University of Colorado Denver and the National Center for Atmospheric Research. Aspects of this research were supported by NSF grants EAR-1252085 and EAR-1246925 at the University of Colorado at Boulder.

FIGURE CAPTIONS

Figure 1. (a) Graphical depiction of a tilted hexagonally symmetric medium with definitions of the foliation plane, symmetry axis, strike angle, and dip angle. (b) Illustrative computation of the variation of apparent S-wave radial (red curve) and SV-wave azimuthal (blue curve) anisotropy as a function of dip angle θ. All amplitudes are normalized.by the amplitude of maximum inherent S-wave anisotropy, These quantities are defined by Equations (9) and (11) in the text, and they are obtained by rotating a hexagonally symmetric elasticity tensor based on the effective anisotropic medium theory (*Montagner and Nataf*, 1986). This figure aims to qualitatively summarize the variation of anisotropy with dip angle,.Details (e.g., the absolute amplitude, the zero-crossing angle, and the number of crossing angles) will depend on the elasticity tensor.

Figure 2. Examples of 10-, 32-, and 50-sec-period Rayleigh wave phase velocity observations as a function of azimuth for location A identified in Fig. 3a. Blue dashed lines give the best fitting 2ψ curves.

Figure 3. The Rayleigh and Love wave isotropic phase speed maps. (a)-(c) Rayleigh wave phase speed maps at 10, 32, and 70 sec period. The 10 sec map comes from ambient noise data, the 40 sec map from a combination of ambient noise and earthquake data, and the 70 sec map comes from earthquake data. (d)-(f) Love wave phase speed maps at 10, 25, and 45 sec period. The 10 sec map is from ambient noise data, the 25 sec map is from a combination of ambient noise and earthquake data, and the 45 sec map comes from earthquake data.

Figure 4. The Rayleigh wave 2ψ azimuthal anisotropy maps. (a)-(c) Rayleigh wave

azimuthal anisotropy maps at 10, 32, and 50 sec period. The 10 sec map comes from ambient noise data, the 32 sec map is from a combination of ambient noise and earthquake data, and the 50 sec map comes from earthquake data. The bars are Rayleigh wave fast directions with lengths representing the peak to peak amplitude (in percent).

Figure 5. Uncertainty maps for (a) the azimuthally isotropic Rayleigh wave phase speeds at 32 sec period, (b) the azimuthally isotropic Love wave phase speed at 25 sec, (c) the fast azimuth of Rayleigh wave azimuthal anisotropy at 32 sec, and (d) amplitude of Rayleigh wave azimuthal anisotropy at 32 sec.

Figure 6. (a-c) The local dispersion curves for Point A in the Basin and Range province (identified in **Fig. 3a**). The local (a) phase speed, (b) fast azimuth direction, and (c) azimuthal anisotropy amplitude curves are presented as one-standard deviation error bars. Red error bars are the Love wave data and blue error bars are the Rayleigh wave data. The solid and dashed lines are the dispersion curves computed from the average of the model ensemble for Point A: solid lines are from Group 1 models while dashed lines are from Group 2 models. (d-f) Similar to (a-c) but for Point B in Colorado Plateau (**Fig. 3a**).

Figure 7. Prior and posterior distributions for several model parameters at 20 km depth for Point A (in the Basin and Range, identified in **Fig. 3a**). White histograms indicate the prior distributions; both blue and red histograms are the posterior distributions but result from the two different model groups.

Figure 8. Similar to **Fig. 7** but for Point B in the Colorado Plateau (**Fig. 3a**).

Figure 9. (a) Group 1 model ensemble at Point A showing the inherent Vsv (blue) and Vsh (red), where the one-standard deviation model distribution is shown with the gray corridors

and the average of each ensemble is plotted with bold lines. (b) Same as (a), but for Group 2, Point A. (c) Same as (a), but for Group 1, Point B. (d) Same as (a), but for Group 2, Point B. Points A and B are identified in **Fig. 3a**.

Figure 10. Aspects of the correlation matrix observed at Point A. (a) The correlations between several model parameters at 20 km depth. (b) The correlations between Vsv at different depths. (c-h) Similar to (b), but for six other model parameters: Vsh, Vpv, Vph, η, θ, and ϕ.

Figure 11. Map view of the crustal averaged non-ellipticity of anisotropy ($\varepsilon - \delta$), the crustal averaged inherent S-wave anisotropy, the crustal dip and strike angles for Group 1 (a-c) and Group 2 (d-f) models. In (c) and (f), the dip angles are represented by the background color and the strike angle directions are given by the black bars. Average values across each map are inset.

Figure 12. Uncertainties for the model variables shown in **Fig. 11**. Average uncertainties across each map are inset.

Figure 13. The spatially averaged inherent S-wave anisotropy as a function of depth. The middle of the error bar is the average amplitude of the inherent S-wave anisotropy, γ, in percent and the half width of the error bar is the spatial average of the one-standard deviation uncertainty. The blue dashed line indicates 4% anisotropy, which is the amplitude of anisotropy averaged over the whole crystalline crust and over the study region. The depth is indicated as a percent of local crustal thickness.

Figure 14. Phase velocity surfaces of Vs1, Vs2, and Vp for two elastic tensors with hexagonal symmetry, one is elliptical (a-c, represents Group 1 model), and the other one is

non-elliptical (d-f, represents Group 2 model). Vs1 polarizations are indicated in (a) and (c), the black bars are the projection of Vs1 vector onto plane of stereonet. The orientations of the two elastic tensor groups are shown at the right hand side of the figure.

Figure 15. Azimuthal velocity variations of the horizontally propagating (a) S_2 wave and (b) P wave where all the velocities are normalized. The red and blue dots represent the velocities computed from the elasticity tensor of Group 1 and Group 2, respectively (the velocities at the edge of Fig. 14b, d). The thick line indicates the strike direction, red for Group 1 and blue for Group 2.

Figure 16. (Red dots) Comparison between the Group 2 strike angle (ϕ_2) and the Group 1 strike angle (ϕ_1), where the red line represents $y=x+90°$. The strike angles in the two groups are estimated to be approximately orthogonal. (Blue dots) Comparison between the fast azimuth of the Rayleigh wave at 16 sec and the Group 1 strike angle, where the blue line represents $y=x$. Crustal sensitive Rayleigh wave fast axis directions are approximately parallel to Group 1 strike directions and perpendicular to Group 2 strike directions.

Figure 17. The mean of the posterior distribution of apparent S-wave radial anisotropy, $\hat{\gamma}$, averaged vertically across the crust for (a) Group 1 models and (b) Group 2 models. Average values are inset.

Figure 18. Prior and posterior distributions for several model parameters at 60 km depth for Point A (in Basin and Range, identified in **Fig. 3a**). Similar to **Fig. 7**, white histograms indicate the prior distributions and red histograms represent the posterior distributions.

Table 1. The mean and standard deviations for the posterior distributions in **Figure 7, 8**

		$\sqrt{L/\rho} = \mathrm{V}_{SV}$ (km/s)	$\sqrt{N/\rho} = \mathrm{V}_{SH}$ (km/s)	$\sqrt{C/\rho} = V_{PV}$ (km/s)	$\sqrt{A/\rho} = V_{PH}$ (km/s)	Dip angle θ (º)	Strike angle ϕ (º)	F/(A-2L)= η	Non-ellipticity $\varepsilon - \delta$
Point A $\rho = 2.79 g/cm^3$	Group 1	3.57 (0.04)	3.74 (0.06)	6.14 (0.15)	6.52 (0.15)	21 (6)	37 (12)	0.87 (0.07)	-0.01 (0.04)
	Group 2	3.54 (0.03)	3.72 (0.07)	6.15 (0.13)	6.47 (0.18)	22 (7)	126 (13)	0.74 (0.05)	0.06 (0.02)
Point B $\rho = 2.73 g/cm^3$	Group 1	3.48 (0.04)	3.63 (0.04)	5.94 (0.17)	6.28 (0.18)	34 (7)	19(6)	0.82 (0.06)	0.02 (0.03)
	Group 2	3.45 (0.04)	3.61 (0.04)	6.06 (0.12)	6.24 (0.19)	27 (6)	110 (5)	0.72 (0.03)	0.08 (0.01)

References

Anderson, D. L., and J. Regan (1983), Uppermantle anisotropy and the oceanic lithosphere, Geophys. Res. Lett., 10(9), 841–844, doi:10.1029/GL010i009p00841.

Anderson, D. L., B. Minster, and D. Cole (1974), The effect of oriented cracks on seismic velocities, J. Geophys. Res., 79(26), 4011–4015, doi:10.1029/JB079i026p04011.

Anderson, D. L., and Thomsen, L. (2015), Weak elastic anisotropy in global seismology, submitted to the "Don L. Anderson Tribute" volume, Foulger, G. et al, Eds., to be published by GSA and AGU, 2015.

Auld, B. A. (1973), Acoustic fields and waves in solids, Vol. I, p. 423, Wiley, New York.

Babuška, V. (1991), Seismic Anisotropy in the Earth, Modern approaches in geophysics v. 10, Kluwer Academic Publishers, Dordrecht, The Netherlands□; Boston.

Backus, G. E. (1962), Long-wave elastic anisotropy produced by horizontal layering, J. Geophys. Res., 67(11), 4427–4440, doi:10.1029/JZ067i011p04427.

Bensen, G. D., M. H. Ritzwoller, and Y. Yang (2009), A 3-D shear velocity model of the crust and uppermost mantle beneath the United States from ambient seismic noise, Geophys. J. Int., 177(3), 1177–1196, doi:10.1111/j.1365-246X.2009.04125.x.

Brocher, T. M. (2005), Empirical relations between elastic wavespeeds and eensity in the Earth's crust, Bull. Seismol. Soc. Am., 95(6), 2081–2092, doi:10.1785/0120050077.

Brownlee, S. J., B. R. Hacker, M. Salisbury, G. Seward, T. A. Little, S. L. Baldwin, and G. A. Abers (2011), Predicted velocity and density structure of the exhuming Papua New Guinea ultrahigh-pressure terrane, J. Geophys. Res. Solid Earth, 116(B8), B08206, doi:10.1029/2011JB008195.

Carcione, J. J. M. (2007), Wave Fields in Real Media: Wave Propagation in Anisotropic, Anelastic, Porous and Electromagnetic Media, Elsevier.

Chapman, A. D., S. Kidder, J. B. Saleeby, and M. N. Ducea (2010), Role of extrusion of the Rand and Sierra de Salinas schists in Late Cretaceous extension and rotation of the southern Sierra Nevada and vicinity, Tectonics, 29(5), TC5006, doi:10.1029/2009TC002597.

Christensen, N. I. (1984), The magnitude, symmetry and origin of upper mantle anisotropy based on fabric analyses of ultramafic tectonites, Geophys. J. Int., 76(1), 89–111, doi:10.1111/j.1365-246X.1984.tb05025.x.

Christensen, N. I., and W. D. Mooney (1995), Seismic velocity structure and composition of the continental crust: A global view, J. Geophys. Res. Solid Earth, 100(B6), 9761–9788, doi:10.1029/95JB00259.

Crampin, S. (1984), Effective anisotropic elastic constants for wave propagation through cracked solids, Geophys. J. Int., 76(1), 135–145, doi:10.1111/j.1365-246X.1984.tb05029.x.

Dziewoński, A. M., and D. L. Anderson (1981), Preliminary reference Earth model, Phys. Earth Planet. Inter., 25(4), 297–356, doi:10.1016/0031-9201(81)90046-7.

Ekström, G., and A. M. Dziewoński (1998), The unique anisotropy of the Pacific upper mantle, Nature, 394(6689), 168–172, doi:10.1038/28148.

Ekström, G. (2013), Love and Rayleigh phase-velocity maps, 5–40 s, of the western and central USA from USArray data, Earth Planet. Sci. Lett., doi:10.1016/j.epsl.2013.11.022.

Erdman, M. E., B. R. Hacker, G. Zandt, and G. Seward (2013), Seismic anisotropy of the crust: electron-backscatter diffraction measurements from the Basin and Range, Geophys. J. Int., 195(2), 1211–1229, doi:10.1093/gji/ggt287.

Gung, Y., M. Panning, and B. Romanowicz (2003), Global anisotropy and the thickness of continents, Nature, 422(6933), 707–711, doi:10.1038/nature01559.

Hacker, B.R., M.H. Ritzwoller, and J. Xie, Central Tibet has a partially melted, mica-bearing crust, *Tectonics*, 33, doi:10.1002/2014TC003534, 2014.

Helbig, K., and L. Thomsen (2005), 75-plus years of anisotropy in exploration and reservoir seismics: A historical review of concepts and methods, GEOPHYSICS, 70(6), 9ND–23ND, doi:10.1190/1.2122407.

Huang, H., H. Yao, and R. D. van der Hilst (2010), Radial anisotropy in the crust of SE Tibet and SW China from ambient noise interferometry, Geophys. Res. Lett., 37, 5 PP., doi:201010.1029/2010GL044981.

Jacobson, C. E. (1983), Structural geology of the Pelona Schist and Vincent thrust, San Gabriel Mountains, California, Geol. Soc. Am. Bull., 94(6), 753–767, doi:10.1130/0016-7606(1983)94<753:SGOTPS>2.0.CO;2.

Jacobson, C. E., M. Grove, A. Vucic, J. N. Pedrick, and K. A. Ebert (2007), Exhumation of the Orcopia Schist and associated rocks of southeastern California: Relative roles of erosion, synsubduction tectonic denudation, and middle Cenozoic extension, Geological Society of America Special Paper 419, 1-37.

John, B. E., and D. A. Foster (1993), Structural and thermal constraints on the initiation angle of detachment faulting in the southern Basin and Range: The Chemehuevi Mountains case study, Geol. Soc. Am. Bull., 105(8), 1091–1108, doi:10.1130/0016-7606(1993)105<1091:SATCOT>2.3.CO;2.

Johnson, R. A., and K. L. Loy (1992), Seismic reflection evidence for seismogenic low-angle faulting in southeastern Arizona, Geology, 20(7), 597–600, doi:10.1130/0091-7613(1992)020<0597:SREFSL>2.3.CO;2.

Kawakatsu, H., P. Kumar, Y. Takei, M. Shinohara, T. Kanazawa, E. Araki, and K. Suyehiro (2009), Seismic evidence for sharp lithosphere-asthenosphere boundaries of oceanic plates, Science, 324(5926), 499–502, doi:10.1126/science.1169499.

Kennett, B. L. N., E. R. Engdahl, and R. Buland (1995), Constraints on seismic velocities in the Earth from traveltimes, Geophys. J. Int., 122(1), 108–124, doi:10.1111/j.1365-246X.1995.tb03540.x.

Kustowski, B., G. Ekström, and A. M. Dziewoński (2008), Anisotropic shear-wave velocity structure of the Earth's mantle: A global model, J. Geophys. Res. Solid Earth, 113(B6), B06306, doi:10.1029/2007JB005169.

Lin, F.-C., and M. H. Ritzwoller (2011), Helmholtz surface wave tomography for isotropic and azimuthally anisotropic structure, Geophys. J. Int., 186(3), 1104–1120, doi:10.1111/j.1365-246X.2011.05070.x.

Lin, F.-C., M. H. Ritzwoller, and R. Snieder (2009), Eikonal tomography: surface wave tomography by phase front tracking across a regional broad-band seismic array, Geophys. J. Int., 177(3), 1091–1110, doi:10.1111/j.1365-246X.2009.04105.x.

Lin, F.-C., M. H. Ritzwoller, Y. Yang, M. P. Moschetti, and M. J. Fouch (2011), Complex and variable crustal and uppermost mantle seismic anisotropy in the western United States, Nat. Geosci., 4(1), 55–61, doi:10.1038/ngeo1036.

Masters, G., M. P. Barmine, and S. Kientz (2007), Mineos user's manual, in Computational Infrastructure for Geodynamics, Calif. Inst. of Technol., Pasadena.

Malavieille, J. (1993), Late Orogenic extension in mountain belts: Insights from the basin and range and the Late Paleozoic Variscan Belt, Tectonics, 12(5), 1115–1130, doi:10.1029/93TC01129.

Marone, F., and B. Romanowicz (2007), The depth distribution of azimuthal anisotropy in the continental upper mantle, Nature, 447(7141), 198–201, doi:10.1038/nature05742.

Meissner, R., W. Rabbel, and H. Kern (2006), Seismic lamination and anisotropy of the Lower Continental Crust, Tectonophysics, 416(1–4), 81–99, doi:10.1016/j.tecto.2005.11.013.

Montagner, J.-P., and D. L. Anderson (1989), Constrained reference mantle model, Phys. Earth Planet. Inter., 58(2–3), 205–227, doi:10.1016/0031-9201(89)90055-1.

Montagner, J.-P., and H.-C. Nataf (1986), A simple method for inverting the azimuthal anisotropy of surface waves, J. Geophys. Res., 91(B1), 511, doi:10.1029/JB091iB01p00511.

Montagner, J.-P., and H.-C. Nataf (1988), Vectorial tomography—I. Theory, Geophys. J., 94(2), 295–307, doi:10.1111/j.1365-246X.1988.tb05903.x.

Moschetti, M. P., M. H. Ritzwoller, F.-C. Lin, and Y. Yang (2010a), Crustal shear wave velocity structure of the western United States inferred from ambient seismic noise and earthquake

data, J. Geophys. Res., 115, 20 PP., doi:2010 10.1029/2010JB007448.

Moschetti, M. P., M. H. Ritzwoller, F. Lin, and Y. Yang (2010b), Seismic evidence for widespread western-US deep-crustal deformation caused by extension, Nature, 464(7290), 885–889, doi:10.1038/nature08951.

Nettles, M., and A. M. Dziewoński (2008), Radially anisotropic shear velocity structure of the upper mantle globally and beneath North America, J. Geophys. Res., 113, 27 PP., doi:200810.1029/2006JB004819.

Okaya, D. A., and N. I. Christensen (2002), Anisotropic effects of non-axial seismic wave propagation in foliated crustal rocks, Geophys. Res. Lett., 29(11), 2–1–2–4, doi:10.1029/2001GL014285.

Okaya, D. A., and T. V. McEvilly (2003), Elastic wave propagation in anisotropic crustal material possessing arbitrary internal tilt, Geophys. J. Int., 153(2), 344–358, doi:10.1046/j.1365-246X.2003.01896.x.

Ribe, N. M. (1992), On the relation between seismic anisotropy and finite strain, J. Geophys. Res. Solid Earth, 97(B6), 8737–8747, doi:10.1029/92JB00551.

Ritzwoller, M. H., F.-C. Lin, and W. Shen (2011), Ambient noise tomography with a large seismic array, Comptes Rendus Geosci., 343(8–9), 558–570, doi:10.1016/j.crte.2011.03.007.

Shapiro, N. M., M. Campillo, L. Stehly, and M. H. Ritzwoller (2005), High-Resolution Surface-Wave Tomography from Ambient Seismic Noise, Science, 307(5715), 1615–1618, doi:10.1126/science.1108339.

Shen, W., M. H. Ritzwoller, V. Schulte-Pelkum, and F.-C. Lin (2013a), Joint inversion of surface wave dispersion and receiver functions: a Bayesian Monte-Carlo approach, Geophys. J. Int., 192(2), 807–836, doi:10.1093/gji/ggs050.

Shen, W., M. H. Ritzwoller, and V. Schulte-Pelkum (2013b), A 3-D model of the crust and uppermost mantle beneath the Central and Western US by joint inversion of receiver functions and surface wave dispersion, J. Geophys. Res. Solid Earth, 118(1), 262–276, doi:10.1029/2012JB009602.

Simons, F. J., R. D. Van Der Hilst, J.-P. Montagner, and A. Zielhuis (2002), Multimode Rayleigh wave inversion for heterogeneity and azimuthal anisotropy of the Australian upper mantle, Geophys. J. Int., 151(3), 738–754, doi:10.1046/j.1365-246X.2002.01787.x.Smith, D. B., M. H. Ritzwoller, and N. M. Shapiro (2004), Stratification of anisotropy in the Pacific upper mantle, J. Geophys. Res. Solid Earth, 109(B11), B11309, doi:10.1029/2004JB003200.

Smith, M. L., and F. A. Dahlen (1973), The azimuthal dependence of Love and Rayleigh wave propagation in a slightly anisotropic medium, J. Geophys. Res., 78(17), 3321–3333, doi:10.1029/JB078i017p03321.

Tatham, D. J., G. E. Lloyd, R. W. H. Butler, and M. Casey (2008), Amphibole and lower crustal

seismic properties, Earth Planet. Sci. Lett., 267(1–2), 118–128, doi:10.1016/j.epsl.2007.11.042.

Thomsen, L. (1986), Weak elastic anisotropy, Geophysics, 51(10), 1954–1966, doi:10.1190/1.1442051.

Wang, N., J.-P. Montagner, A. Fichtner, and Y. Capdeville (2013), Intrinsic versus extrinsic seismic anisotropy: The radial anisotropy in reference Earth models, Geophys. Res. Lett., 40(16), 4284–4288, doi:10.1002/grl.50873.

Weiss, T., S. Siegesmund, W. Rabbel, T. Bohlen, and M. Pohl (1999), Seismic velocities and anisotropy of the Lower Continental Crust: A review, Pure Appl. Geophys., 156(1-2), 97–122, doi:10.1007/s000240050291.

Xiao, H.-B., F. A. Dahlen, and J. Suppe (1991), Mechanics of extensional wedges, J. Geophys. Res. Solid Earth, 96(B6), 10301–10318, doi:10.1029/91JB00222.

Xie, J., M. H. Ritzwoller, W. Shen, Y. Yang, Y. Zheng, and L. Zhou (2013), Crustal radial anisotropy across Eastern Tibet and the Western Yangtze Craton, J. Geophys. Res. Solid Earth, 118(8), 4226–4252, doi:10.1002/jgrb.50296.

Yang, Y., M. H. Ritzwoller, Y. Zheng, W. Shen, A. L. Levshin, and Z. Xie (2012), A synoptic view of the distribution and connectivity of the mid-crustal low velocity zone beneath Tibet, J. Geophys. Res., 117, 20 PP., doi:201210.1029/2011JB008810.

Yao, H., R. D. Van Der Hilst, and M. V. De Hoop (2006), Surface-wave array tomography in SE Tibet from ambient seismic noise and two-station analysis - I. Phase velocity maps, Geophys. J. Int., 166(2), 732–744, doi:10.1111/j.1365-246X.2006.03028.x.

Yao, H., R. D. van der Hilst, and J.-P. Montagner (2010), Heterogeneity and anisotropy of the lithosphere of SE Tibet from surface wave array tomography, J. Geophys. Res., 115(B12), B12307, doi:10.1029/2009JB007142.

Yu, Y., and J. Park (1993), Upper mantle anisotropy and coupled-mode long-period surface waves, Geophys. J. Int., 114(3), 473–489, doi:10.1111/j.1365-246X.1993.tb06981.x.

Yuan, H., and B. Romanowicz (2010), Lithospheric layering in the North American craton, Nature, 466(7310), 1063–1068, doi:10.1038/nature09332.

Yuan, H., B. Romanowicz, K. M. Fischer, and D. Abt (2011), 3-D shear wave radially and azimuthally anisotropic velocity model of the North American upper mantle, Geophys. J. Int., 184(3), 1237–1260, doi:10.1111/j.1365-246X.2010.04901.x.

Zhou, Y., G. Nolet, F. A. Dahlen, and G. Laske (2006), Global upper-mantle structure from finite-frequency surface-wave tomography, J. Geophys. Res. Solid Earth, 111(B4), B04304, doi:10.1029/2005JB003677.

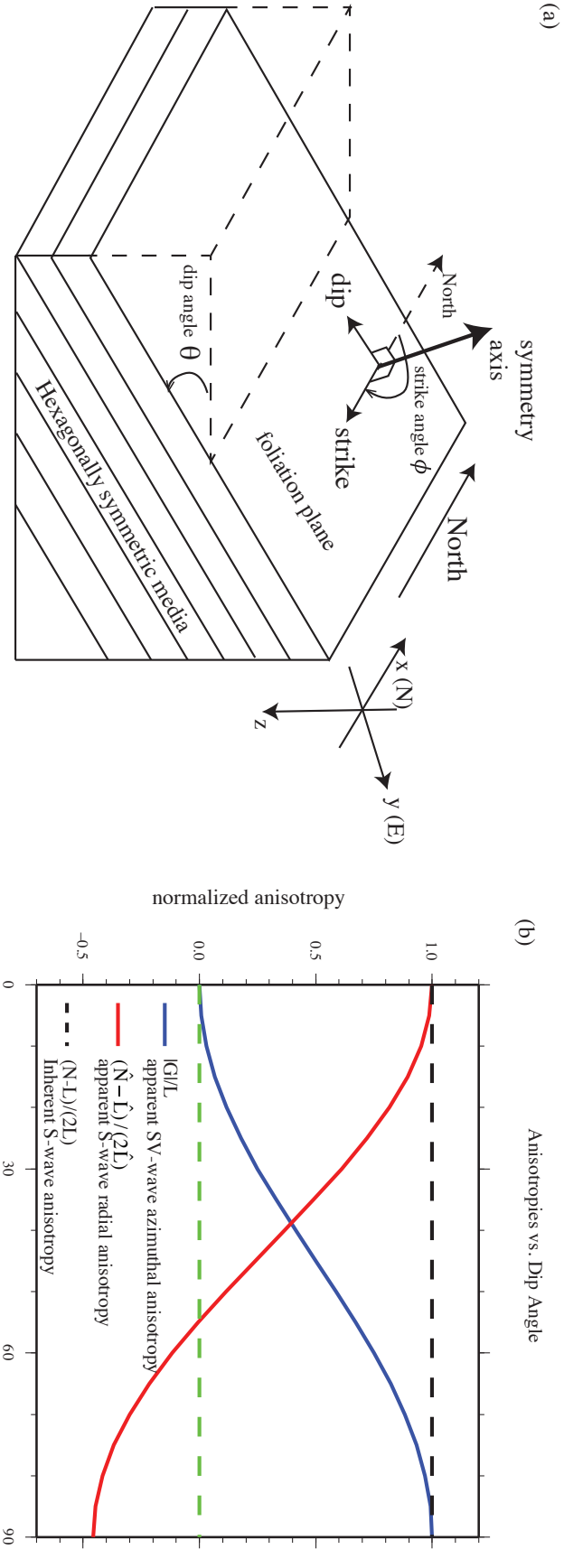
(a)
symmetry axis
North
dip
strike angle ϕ
strike
dip angle θ
foliation plane
Hexagonally symmetric media
North
x (N)
z
y (E)
(b)
Anisotropies vs. Dip Angle
normalized anisotropy
1.0
0.5
0.0
−0.5
0
30
60
90
dip angle θ (deg)
IGI/L
apparent SV-wave azimuthal anisotropy
$(\hat{N}-\hat{L})/(2\hat{L})$
apparent S-wave radial anisotropy
(N-L)/(2L)
Inherent S-wave anisotropy

Figure 1

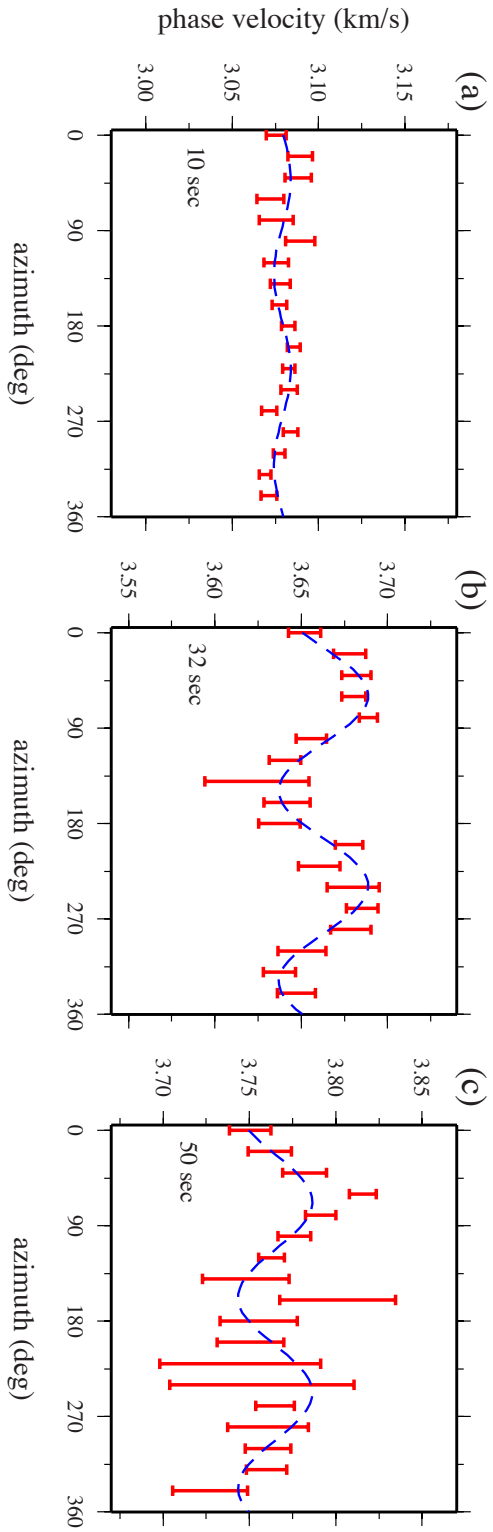
phase velocity (km/s)
(a)
10 sec
azimuth (deg)
(b)
32 sec
azimuth (deg)
(c)
50 sec
azimuth (deg)

Figure 2

Figure 3

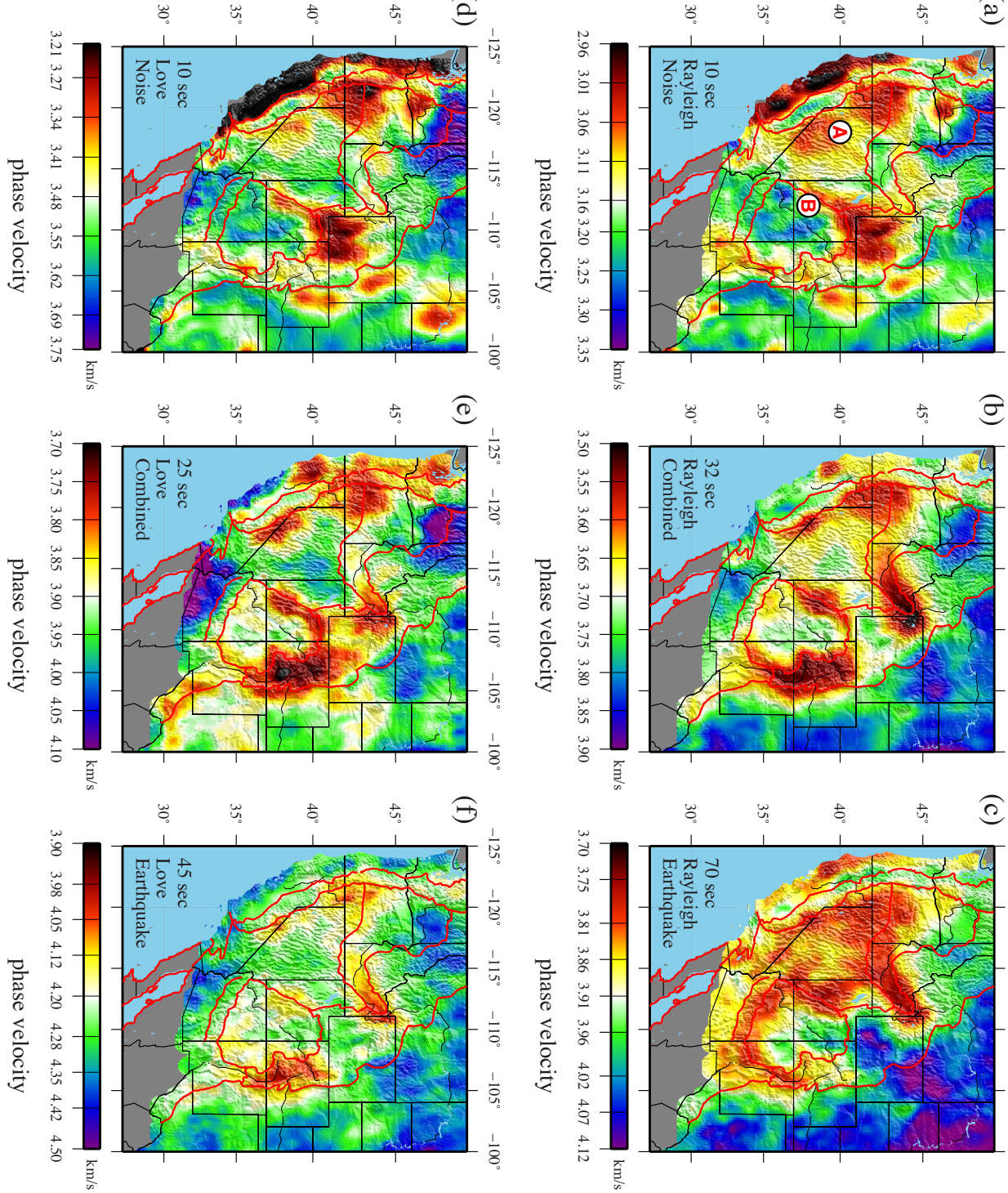
(a)
10 sec Rayleigh Noise
A
B
(b)
32 sec Rayleigh Combined
(c)
70 sec Rayleigh Earthquake
(d)
10 sec Love Noise
(e)
25 sec Love Combined
(f)
45 sec Love Earthquake
phase velocity
km/s

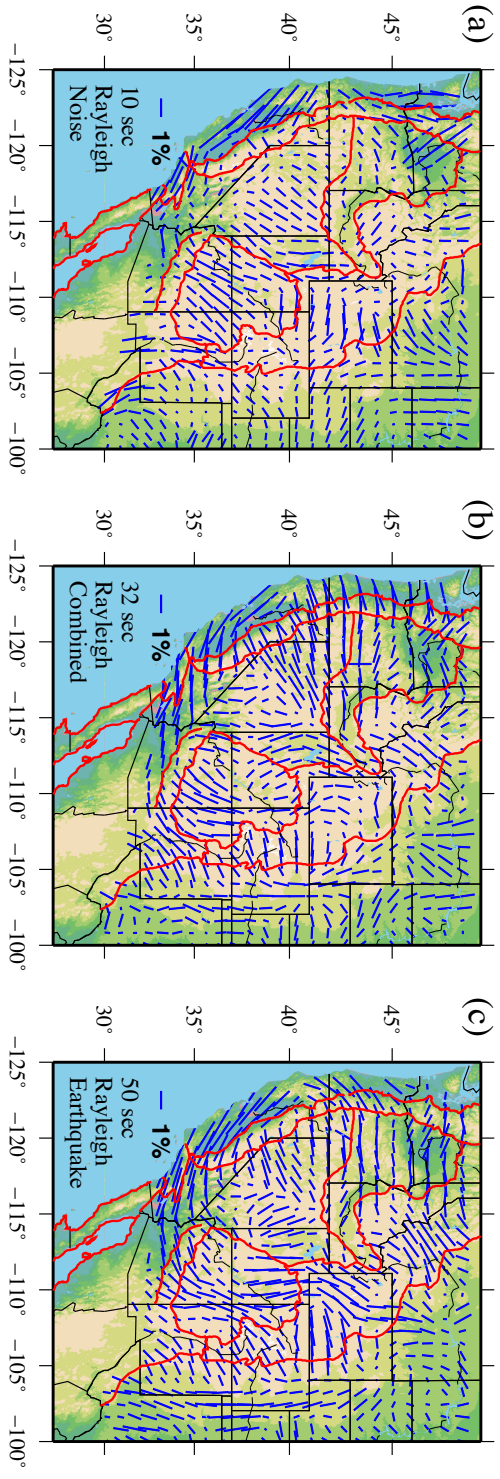
(a)
10 sec
Rayleigh
Noise
1%
(b)
32 sec
Rayleigh
Combined
1%
(c)
50 sec
Rayleigh
Earthquake
1%
30°
35°
40°
45°
−125°
−120°
−115°
−110°
−105°
−100°

Figure 4

Figure 5

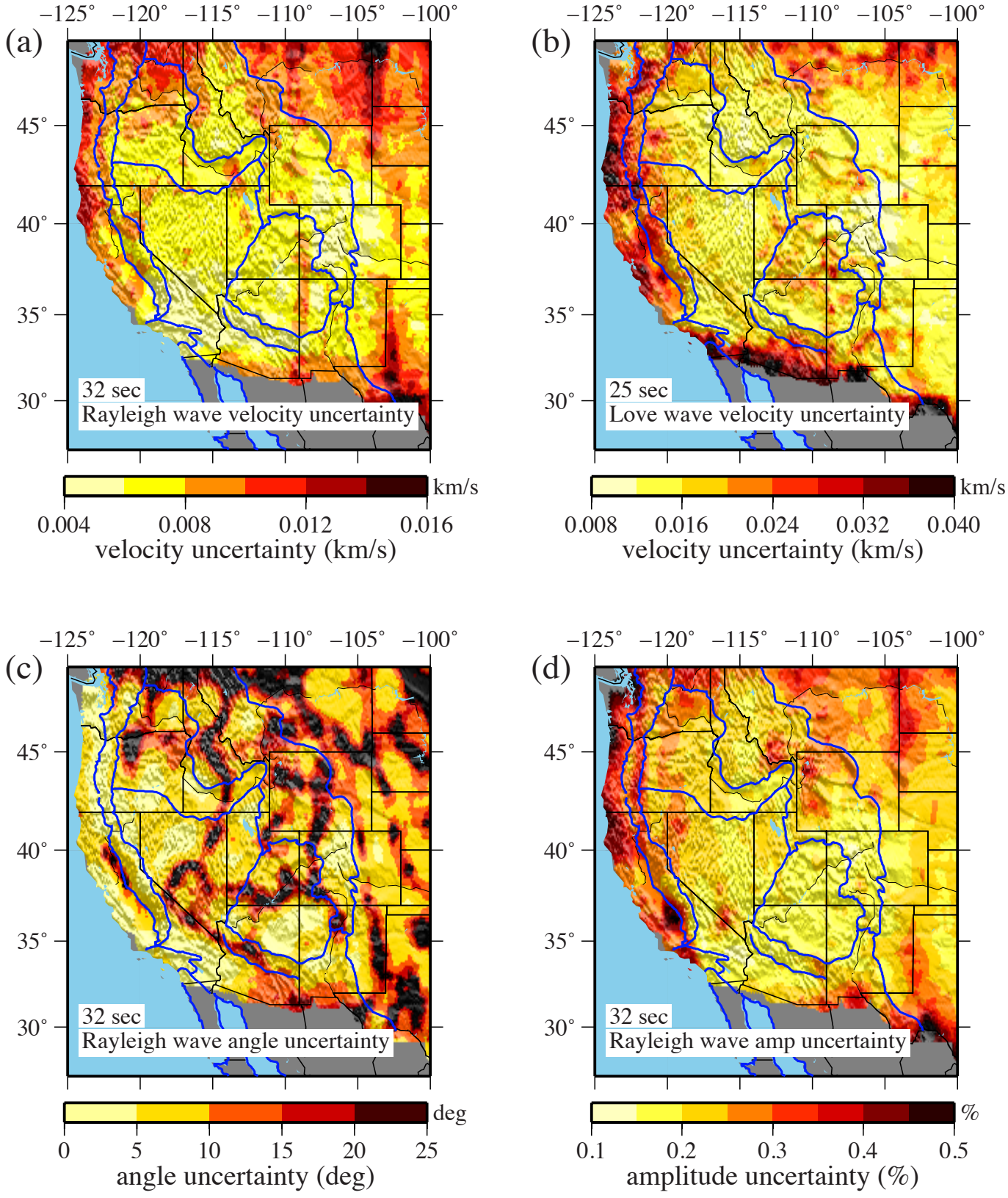
(a)
−125° −120° −115° −110° −105° −100°
45°
40°
35°
30°
32 sec
Rayleigh wave velocity uncertainty
km/s
0.004 0.008 0.012 0.016
velocity uncertainty (km/s)
(b)
−125° −120° −115° −110° −105° −100°
45°
40°
35°
30°
25 sec
Love wave velocity uncertainty
km/s
0.008 0.016 0.024 0.032 0.040
velocity uncertainty (km/s)
(c)
−125° −120° −115° −110° −105° −100°
45°
40°
35°
30°
32 sec
Rayleigh wave angle uncertainty
deg
0 5 10 15 20 25
angle uncertainty (deg)
(d)
−125° −120° −115° −110° −105° −100°
45°
40°
35°
30°
32 sec
Rayleigh wave amp uncertainty
%
0.1 0.2 0.3 0.4 0.5
amplitude uncertainty (%)

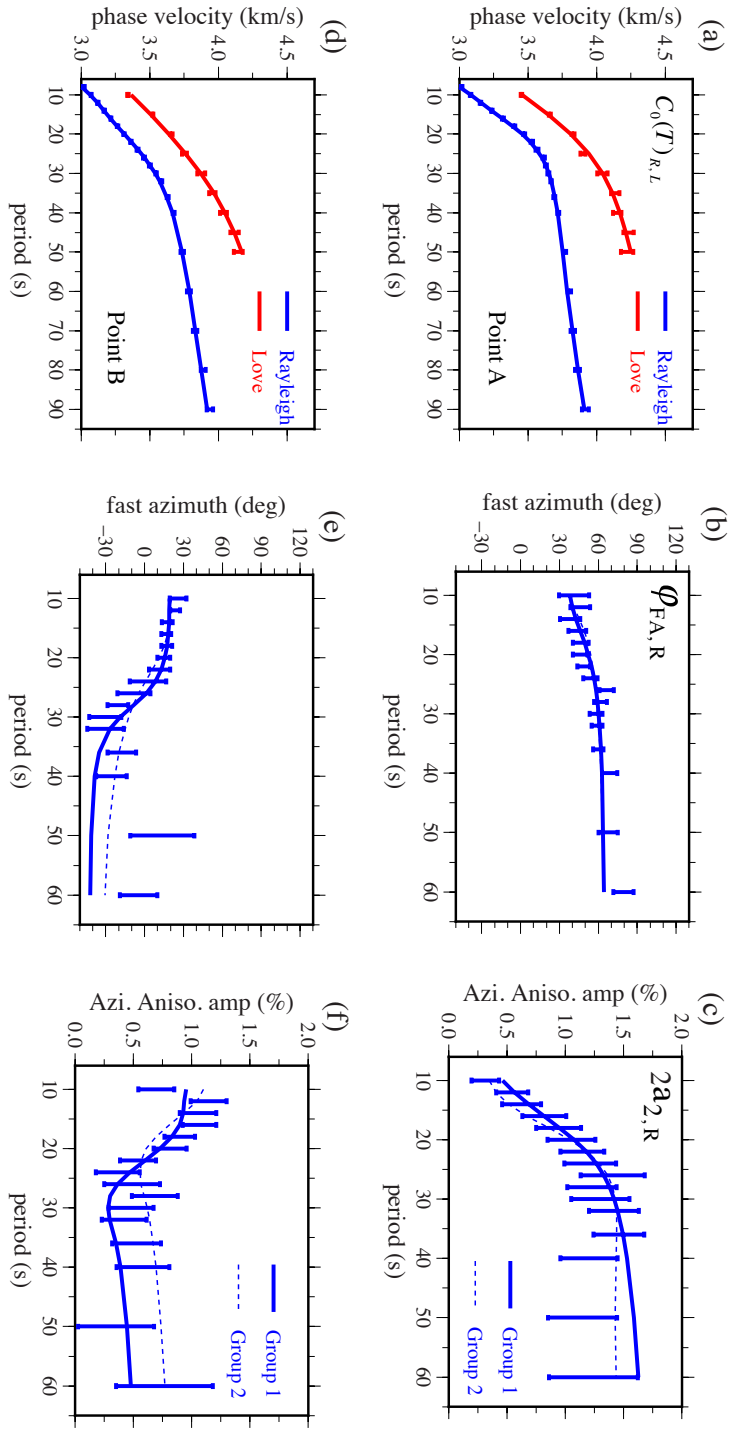
(a)
phase velocity (km/s)
period (s)
$C_0(T)_{R,L}$
Rayleigh
Love
Point A
(b)
fast azimuth (deg)
period (s)
$\varphi_{FA,R}$
(c)
Azi. Aniso. amp (%)
period (s)
$2a_{2,R}$
Group 1
Group 2
(d)
phase velocity (km/s)
period (s)
Point B
Rayleigh
Love
(e)
fast azimuth (deg)
period (s)
(f)
Azi. Aniso. amp (%)
period (s)
Group 1
Group 2

Figure 6

Figure 7 Point A

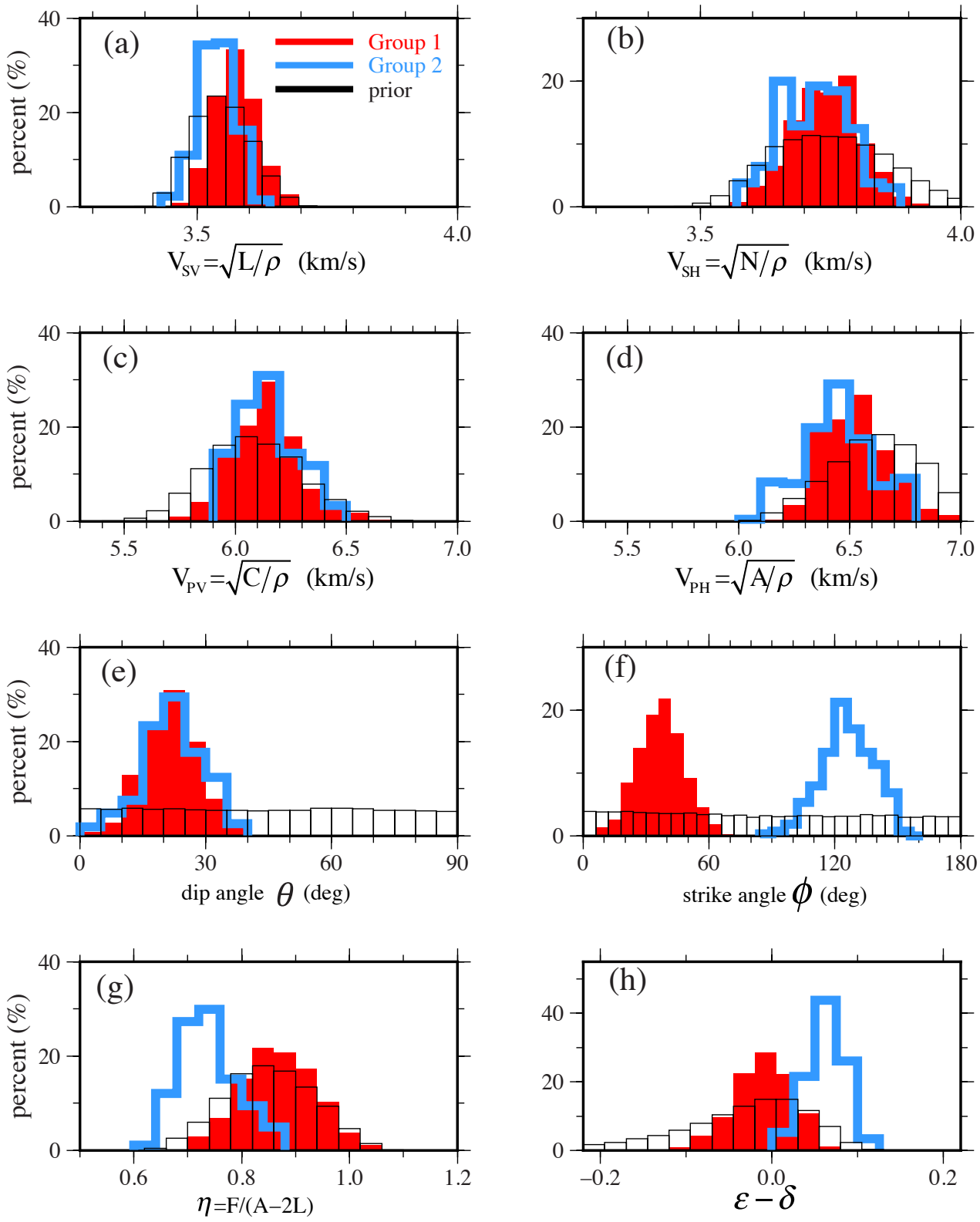

Figure 8 Point B

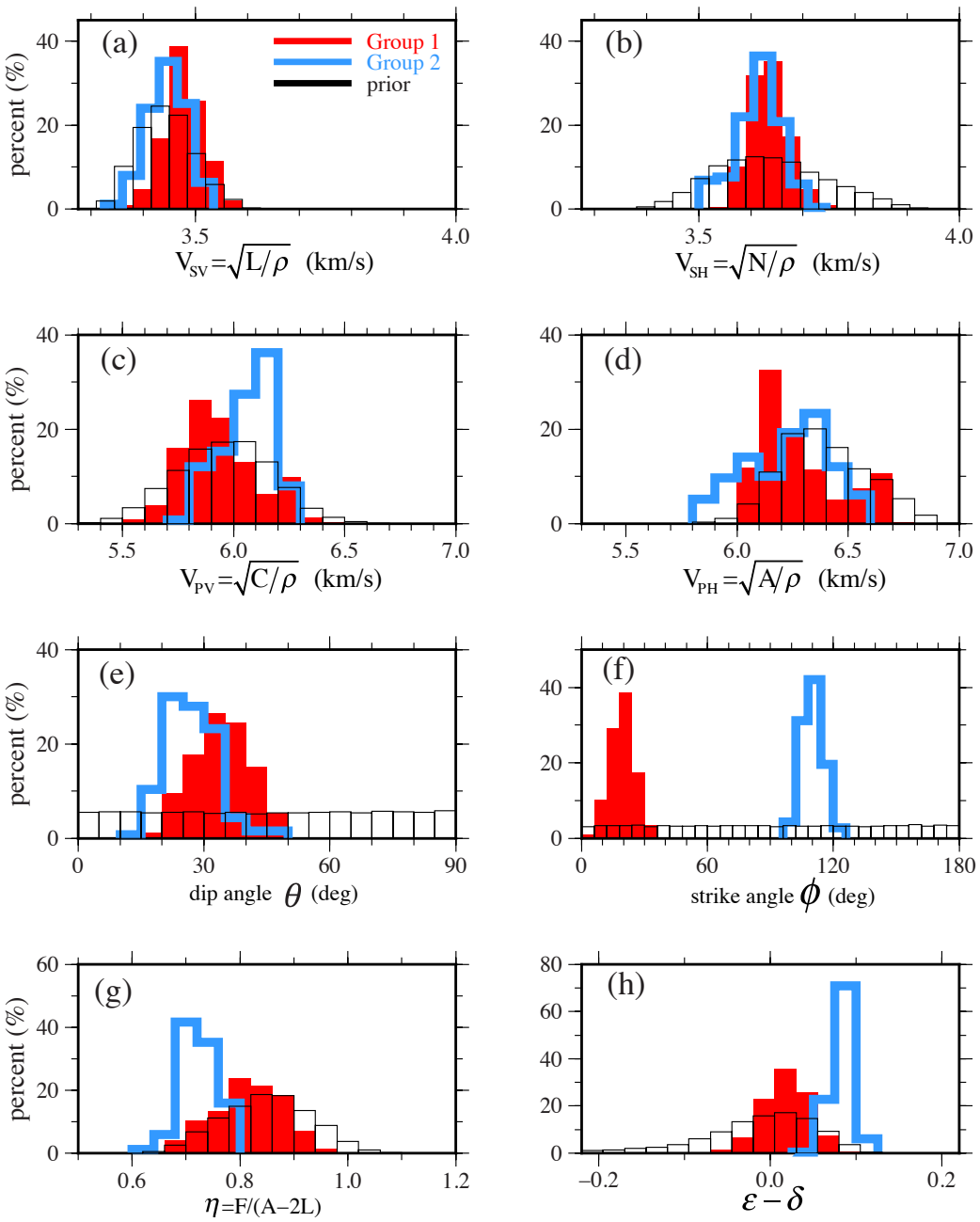

Figure 9

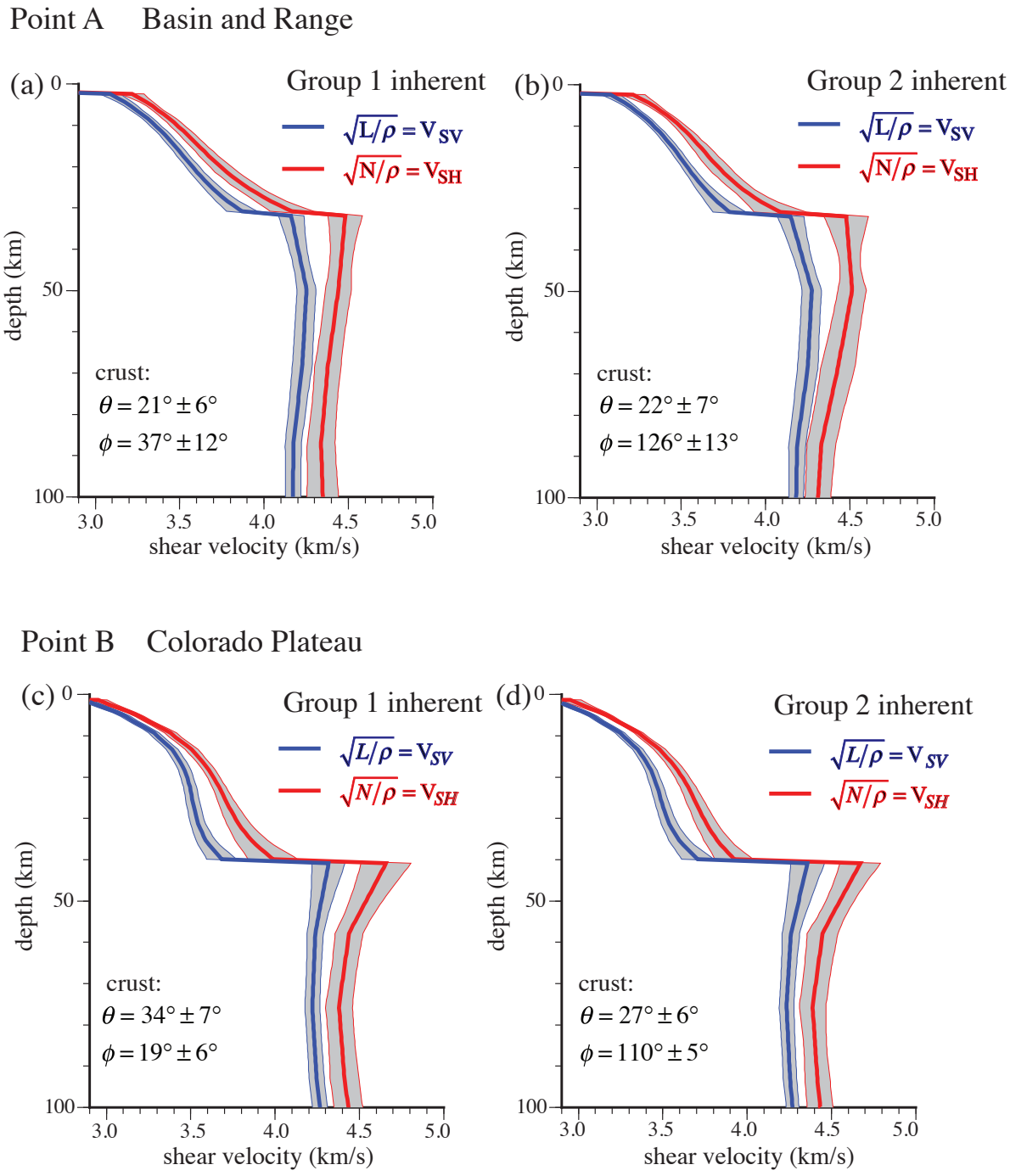
Point A Basin and Range
(a)
Group 1 inherent
$\sqrt{L/\rho} = V_{SV}$
$\sqrt{N/\rho} = V_{SH}$
depth (km)
0
50
100
crust:
$\theta = 21° \pm 6°$
$\phi = 37° \pm 12°$
3.0
3.5
4.0
4.5
5.0
shear velocity (km/s)
(b)
Group 2 inherent
$\sqrt{L/\rho} = V_{SV}$
$\sqrt{N/\rho} = V_{SH}$
depth (km)
0
50
100
crust:
$\theta = 22° \pm 7°$
$\phi = 126° \pm 13°$
3.0
3.5
4.0
4.5
5.0
shear velocity (km/s)
Point B Colorado Plateau
(c)
Group 1 inherent
$\sqrt{L/\rho} = V_{SV}$
$\sqrt{N/\rho} = V_{SH}$
depth (km)
0
50
100
crust:
$\theta = 34° \pm 7°$
$\phi = 19° \pm 6°$
3.0
3.5
4.0
4.5
5.0
shear velocity (km/s)
(d)
Group 2 inherent
$\sqrt{L/\rho} = V_{SV}$
$\sqrt{N/\rho} = V_{SH}$
depth (km)
0
50
100
crust:
$\theta = 27° \pm 6°$
$\phi = 110° \pm 5°$
3.0
3.5
4.0
4.5
5.0
shear velocity (km/s)

Figure 10

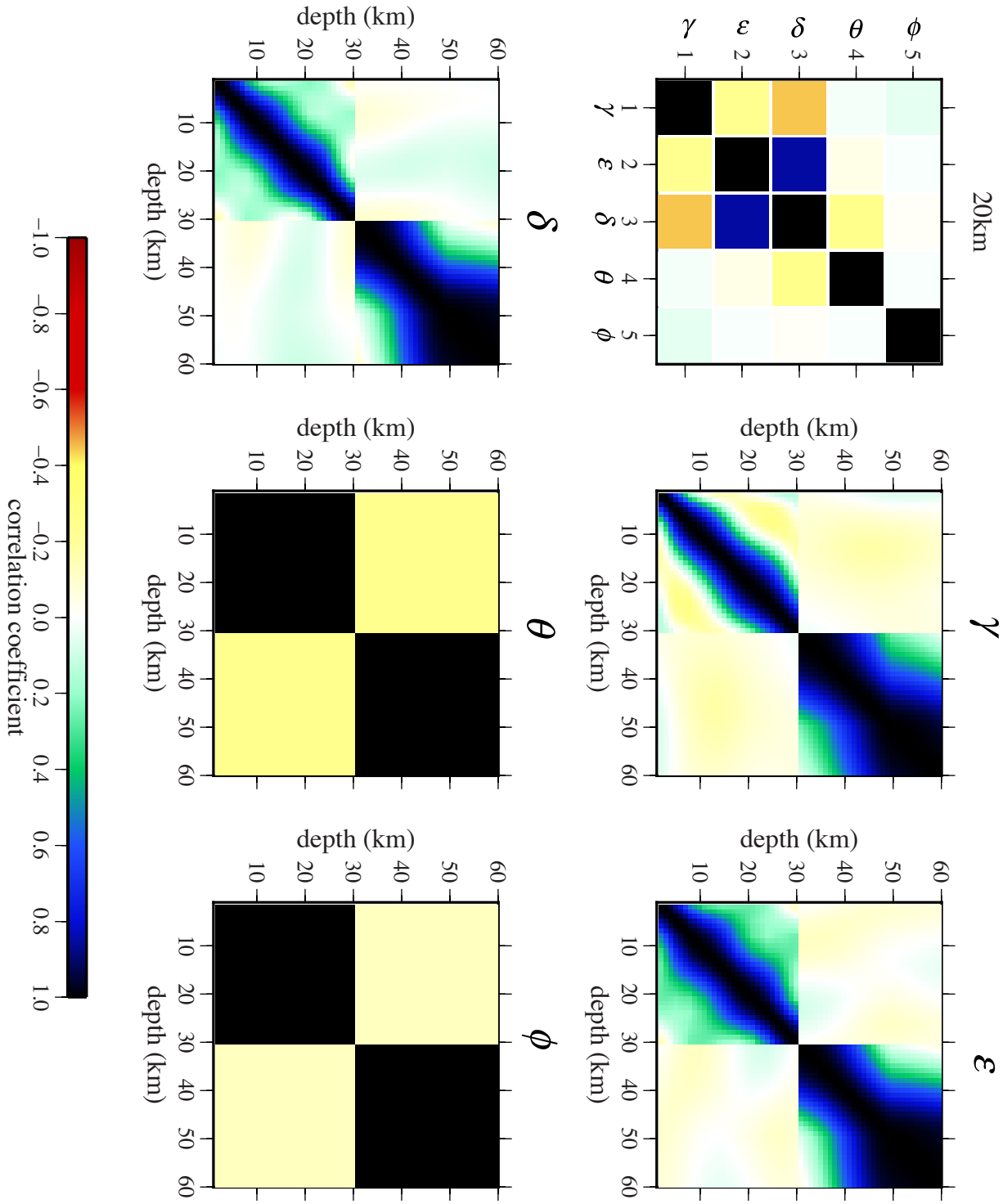
20km
depth (km)
correlation coefficient
−1.0 −0.8 −0.6 −0.4 −0.2 0.0 0.2 0.4 0.6 0.8 1.0

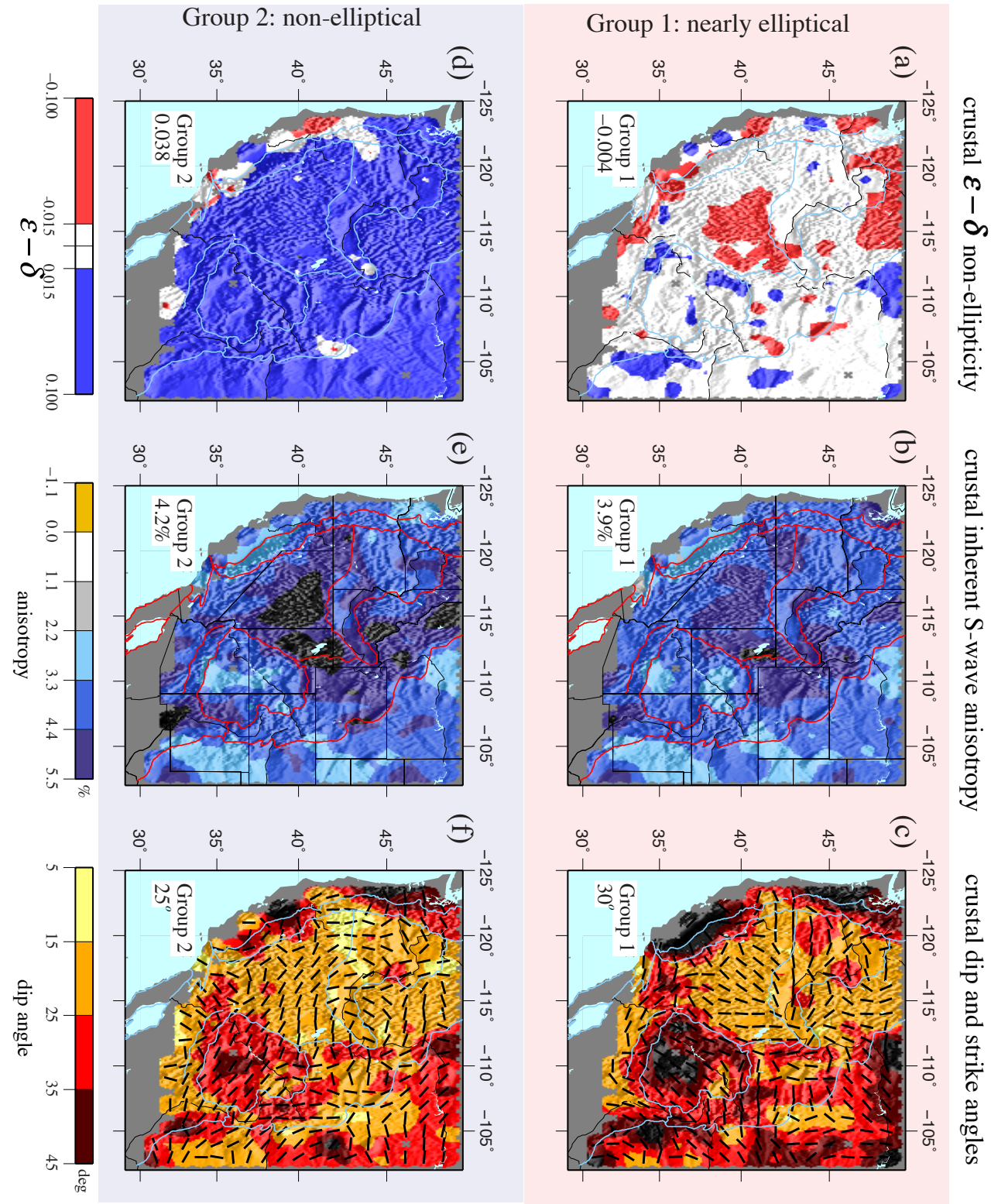
Group 1: nearly elliptical
Group 2: non-elliptical
crustal $\varepsilon - \delta$ non-ellipticity
crustal inherent S-wave anisotropy
crustal dip and strike angles
(a)
(b)
(c)
(d)
(e)
(f)
Group 1 −0.004
Group 1 3.9%
Group 1 30°
Group 2 0.038
Group 2 4.2%
Group 2 25°
−125° −120° −115° −110° −105°
30° 35° 40° 45°
$\varepsilon - \delta$
−0.100 −0.015 0.015 0.100
anisotropy
−1.1 0.0 1.1 2.2 3.3 4.4 5.5
%
dip angle
5 15 25 35 45
deg

Figure 11

Figure 12

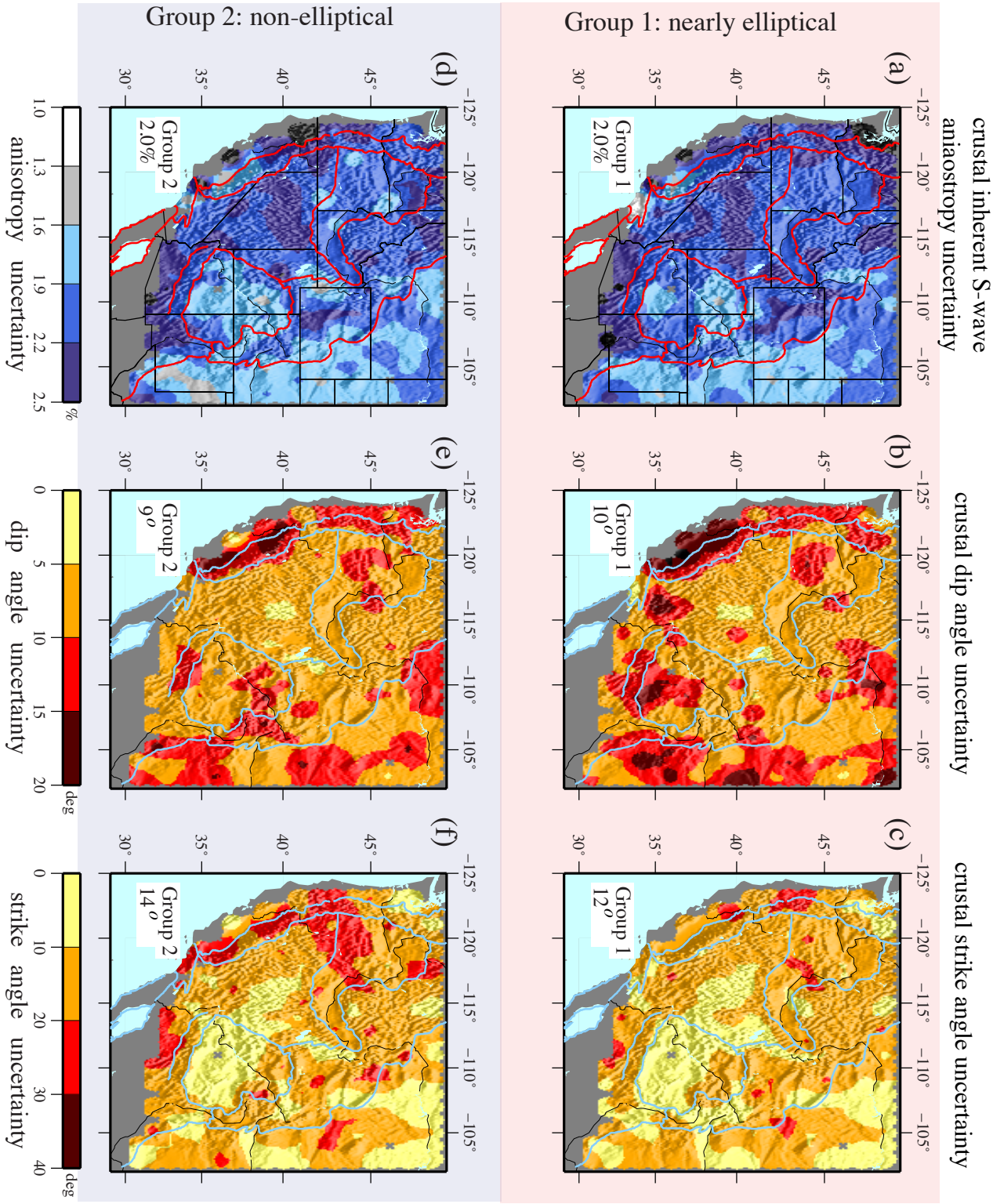
Group 1: nearly elliptical
Group 2: non-elliptical
crustal inherent S-wave aniaostropy uncertainty
crustal dip angle uncertainty
crustal strike angle uncertainty
(a)
(b)
(c)
(d)
(e)
(f)
Group 1 2.0%
Group 2 2.0%
Group 1 10°
Group 2 9°
Group 1 12°
Group 2 14°
anisotropy uncertainty
dip angle uncertainty
strike angle uncertainty
%
deg
deg

Figure 13

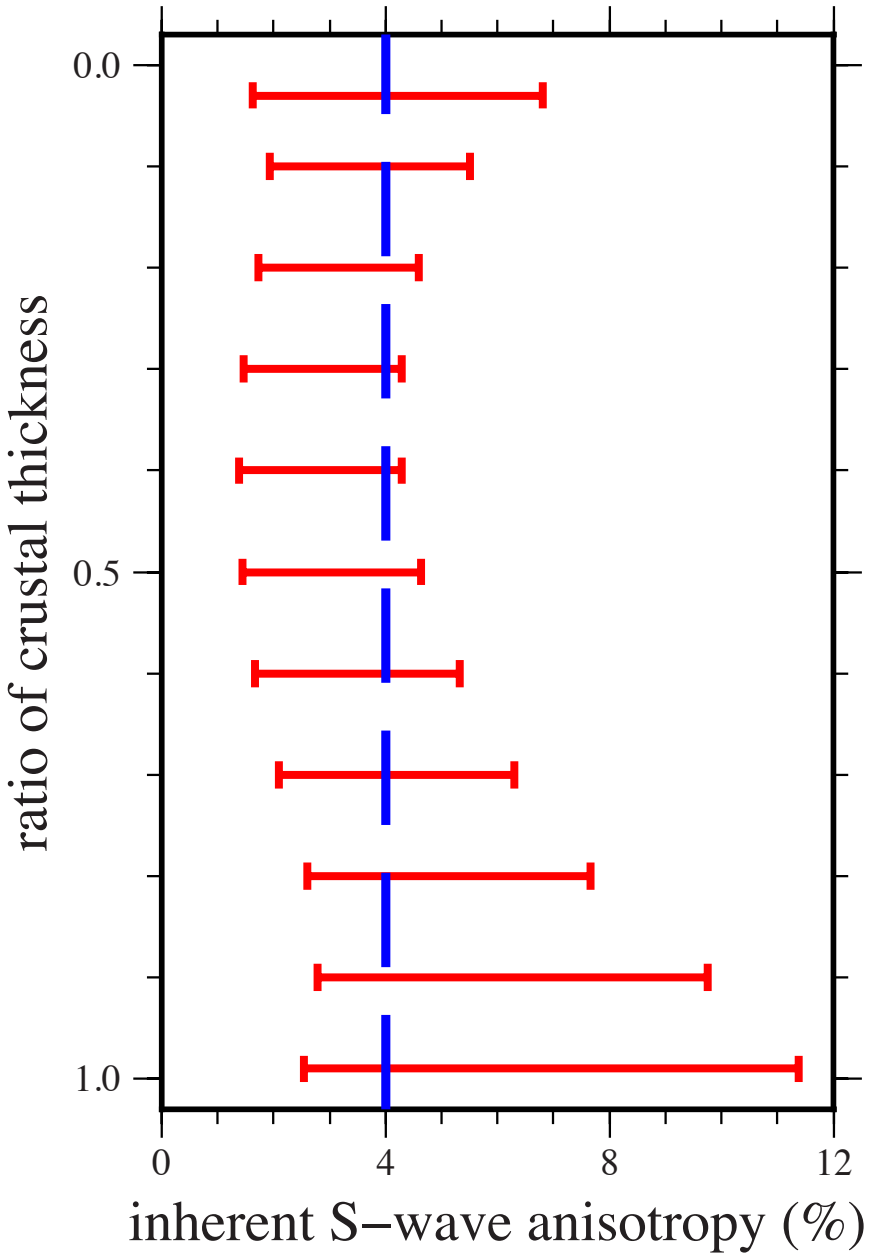
0.0
0.5
1.0
ratio of crustal thickness
0
4
8
12
inherent S−wave anisotropy (%)

Figure 14

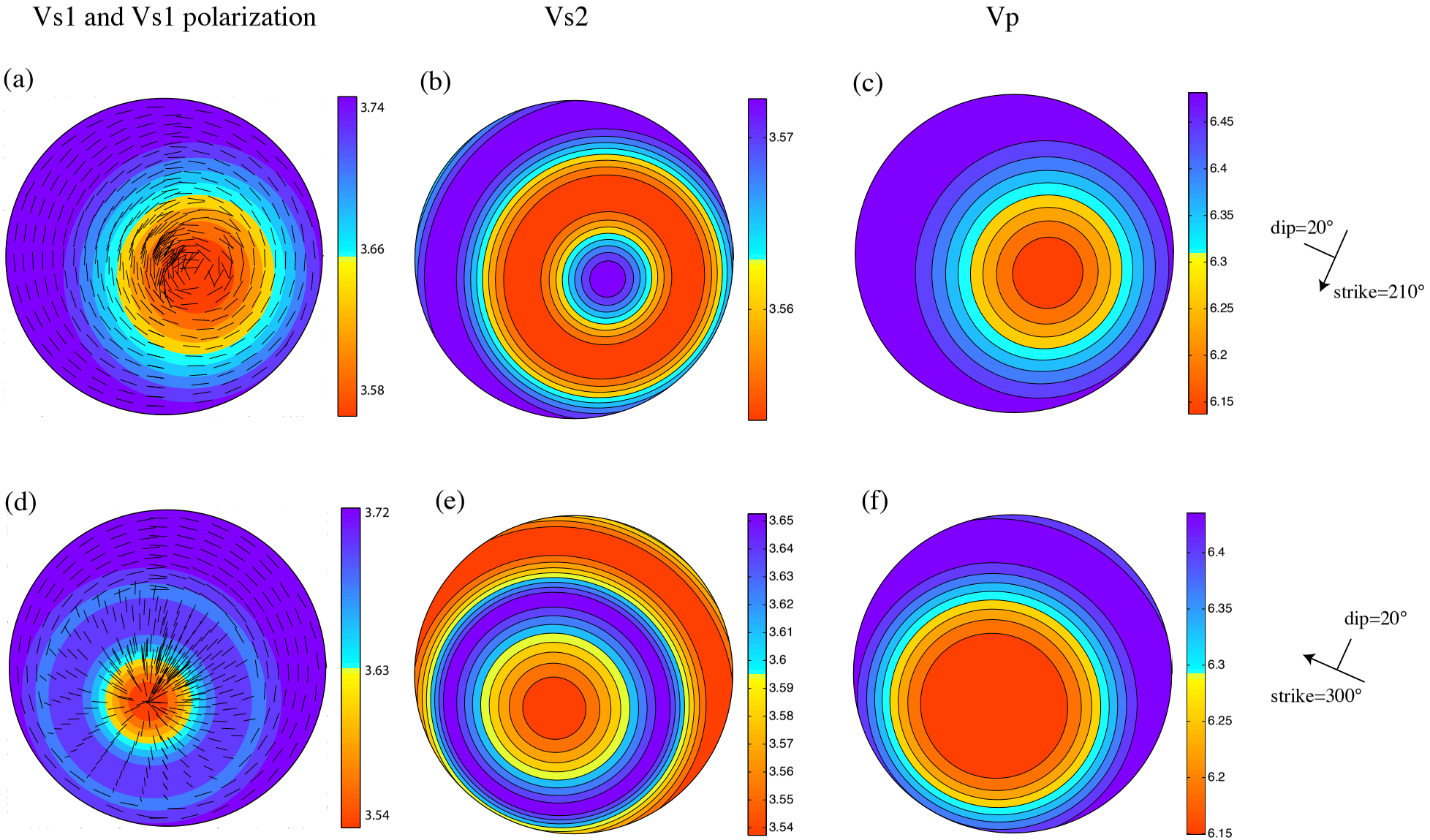
Vs1 and Vs1 polarization
Vs2
Vp
(a)
(b)
(c)
(d)
(e)
(f)
3.74
3.66
3.58
3.57
3.56
6.45
6.4
6.35
6.3
6.25
6.2
6.15
dip=20°
strike=210°
3.72
3.63
3.54
3.65
3.64
3.63
3.62
3.61
3.6
3.59
3.58
3.57
3.56
3.55
3.54
6.4
6.35
6.3
6.25
6.2
6.15
dip=20°
strike=300°

Figure 15

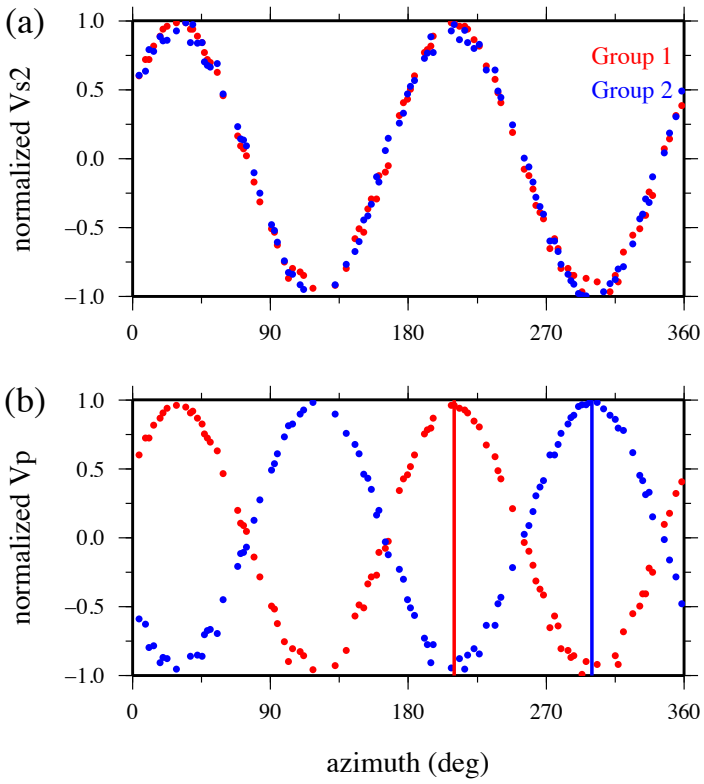
(a)
normalized Vs2
1.0
0.5
0.0
−0.5
−1.0
0
90
180
270
360
Group 1
Group 2
(b)
normalized Vp
azimuth (deg)

Figure 16

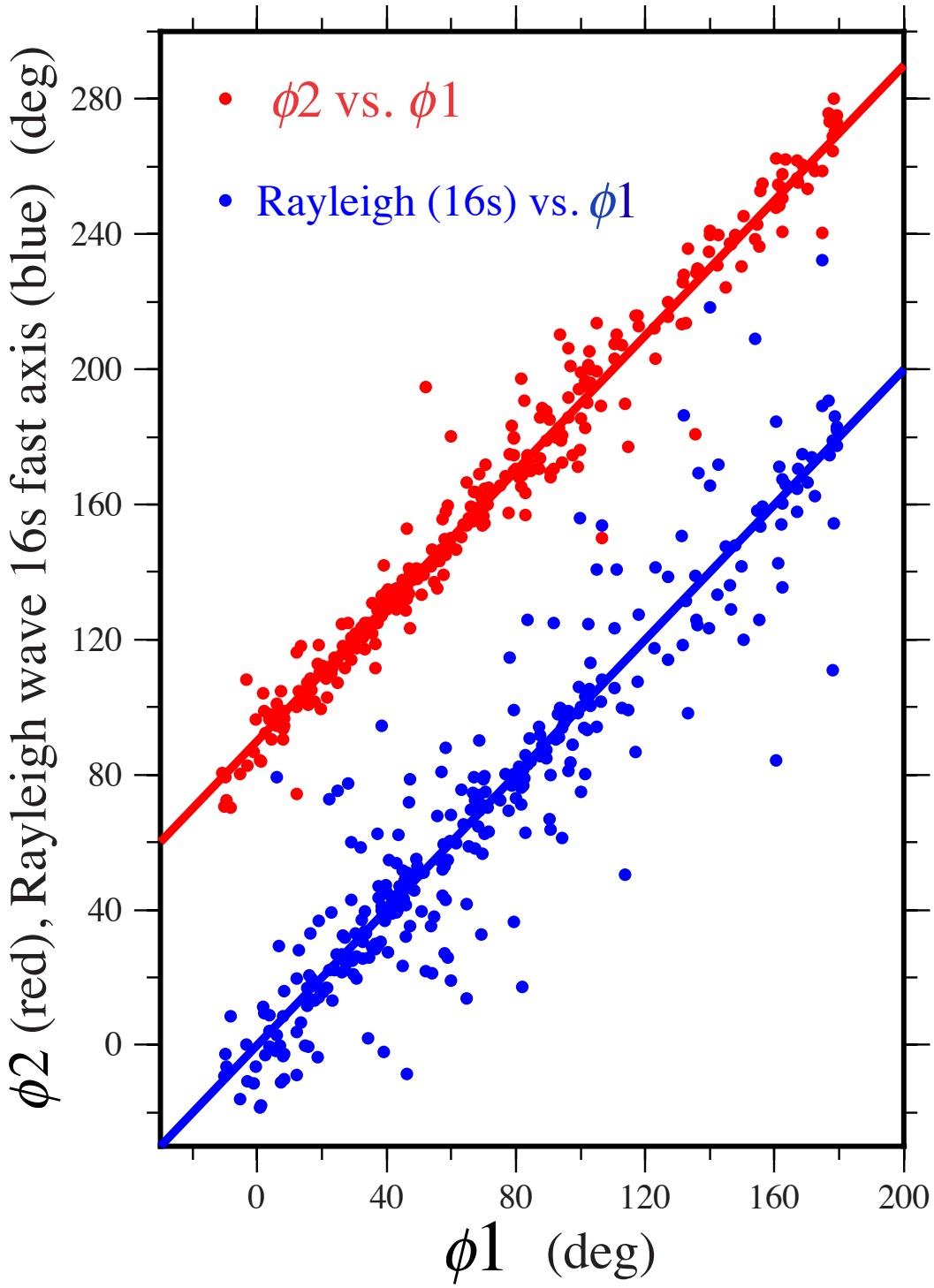
ϕ2 vs. ϕ1
Rayleigh (16s) vs. ϕ1
ϕ2 (red), Rayleigh wave 16s fast axis (blue) (deg)
ϕ1 (deg)
0
40
80
120
160
200
240
280

Figure 17

crustal apparent S-wave radial anisotropy

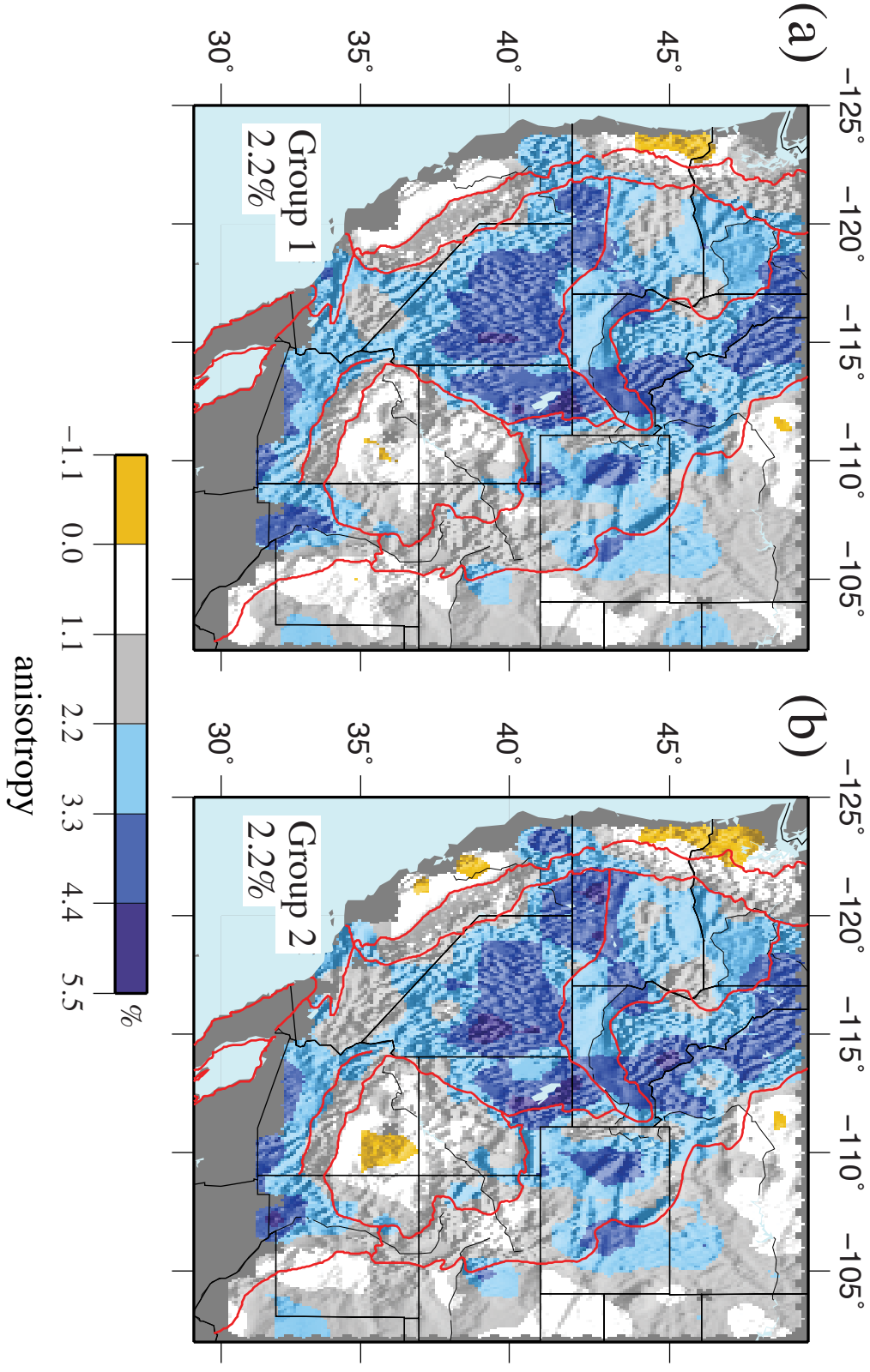

Figure 18

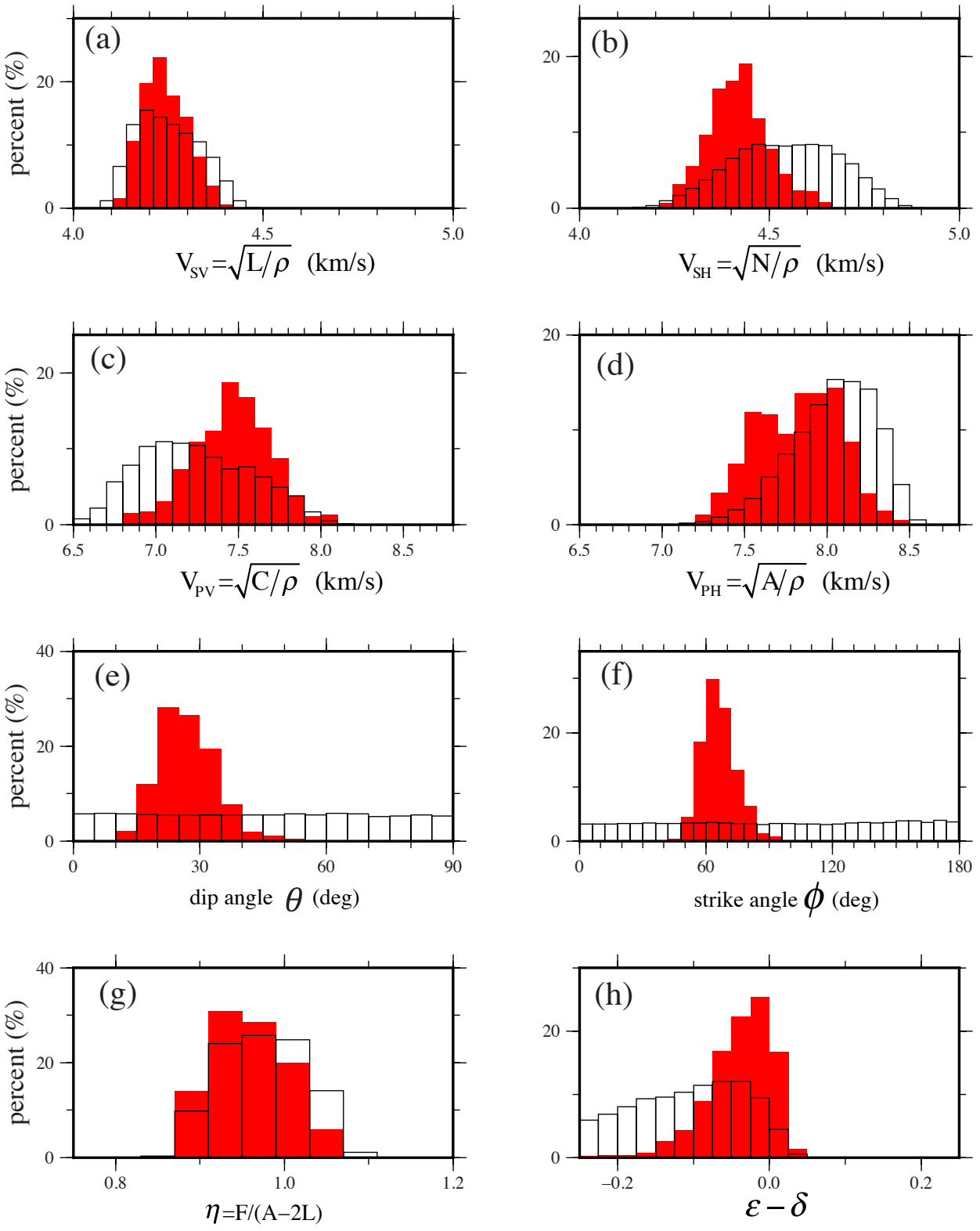
(a)
percent (%)
20
0
4.0
4.5
5.0
$V_{SV}=\sqrt{L/\rho}$ (km/s)
(b)
20
0
4.0
4.5
5.0
$V_{SH}=\sqrt{N/\rho}$ (km/s)
(c)
percent (%)
20
0
6.5
7.0
7.5
8.0
8.5
$V_{PV}=\sqrt{C/\rho}$ (km/s)
(d)
20
0
6.5
7.0
7.5
8.0
8.5
$V_{PH}=\sqrt{A/\rho}$ (km/s)
(e)
percent (%)
40
20
0
0
30
60
90
dip angle θ (deg)
(f)
20
0
0
60
120
180
strike angle ϕ (deg)
(g)
percent (%)
40
20
0
0.8
1.0
1.2
η=F/(A−2L)
(h)
20
0
−0.2
0.0
0.2
$\varepsilon-\delta$

Appendix. The Forward Problem: Computation of period and azimuthally variable phase speeds for an arbitrarily oriented hexagonally symmetric elastic tensor

Given an elastic tensor that varies with depth at a given location, we seek to compute how Rayleigh and Love wave phase velocities change with period T and azimuth ψ. The code MINEOS (*Masters et al*., 2007) computes period dependent Rayleigh and Love wave phase speeds at high accuracy for a transversely isotropic medium; i.e., a medium with hexagonal symmetry and a vertical symmetry axis. Instead, we are interested in a medium whose elastic properties are given by an elastic tensor for a hexagonally symmetric medium with an arbitrarily oriented symmetry axis.

First, let the moduli A, C, N, L, and F represent the elastic tensor at a particular depth for a hexagonally symmetric medium with a vertical symmetry axis, given by Equation (1) in the Introduction. Four of the five moduli are directly related to P and S wave speeds for waves propagating perpendicular or parallel to the symmetry axis using the following relationships: $A = \rho V_{ph}^2, C = \rho V_{pv}^2, L = \rho V_{sv}^2, N = \rho V_{sh}^2$. Here, ρ is density, Vph and Vpv are the speeds of P waves propagating horizontally and vertically respectively, Vsv is the speed of the S wave propagating horizontally and polarized vertically or propagating vertically and polarized horizontally, and Vsh is the speed of the S wave that is propagating in a horizontal direction and polarized horizontally. The modulus $F = \eta(A - 2L)$ affects the speed of waves propagating oblique to the symmetry axis and controls the shape of the shear wave phase speed surface (*Okaya and Christensen*, 2002). For an isotropic medium, $A = C, L = N, F = A - 2L, \eta = 1$.

Next, rotate the tensor in Equation (1) through the two angles, θ (the dip angle) and ϕ (the strike angle), defined in **Figure 1a**, to produce the modulus matrix $C_{\alpha\beta}(\theta,\phi)$. We refer to a general reorientation of the symmetry axis as a tilt, which is achieved by pre- and post-multiplying the elastic modulus matrix by the appropriate Bond rotation matrix and its transpose, respectively (e.g, *Auld*, 1973; *Carcione*, 2007), which act to rotate the 4th-order elasticity tensor appropriately. The order of the rotations matters because the rotation matrices do not commute: first a counter-clockwise rotation through angle θ around the x-axis is applied followed by a second counter-clockwise rotation through angle ϕ around the z-axis. The rotation can fill all components of the modulus matrix but will preserve its symmetry:

$$C_{\alpha\beta}(\theta,\phi)=\begin{bmatrix} C_{11} & C_{12} & C_{13} & C_{14} & C_{15} & C_{16} \\ C_{12} & C_{22} & C_{23} & C_{24} & C_{25} & C_{26} \\ C_{13} & C_{23} & C_{33} & C_{34} & C_{35} & C_{36} \\ C_{14} & C_{24} & C_{34} & C_{44} & C_{45} & C_{46} \\ C_{15} & C_{25} & C_{35} & C_{45} & C_{55} & C_{56} \\ C_{16} & C_{26} & C_{36} & C_{46} & C_{56} & C_{66} \end{bmatrix} \tag{A1}$$

Montagner and Nataf (1986) showed that this modulus matrix may be decomposed into an effective transversely isotropic (azimuthally independent) part, $C_{\alpha\beta}^{ETI}$, and an azimuthally anisotropic part, $C_{\alpha\beta}^{AA}$, as follows:

$$C_{\alpha\beta}(\theta,\phi)=\begin{bmatrix} \hat{A} & \hat{A}-2\hat{N} & \hat{F} & 0 & 0 & 0 \\ \hat{A}-2\hat{N} & \hat{A} & \hat{F} & 0 & 0 & 0 \\ \hat{F} & \hat{F} & \hat{C} & 0 & 0 & 0 \\ 0 & 0 & 0 & \hat{L} & 0 & 0 \\ 0 & 0 & 0 & 0 & \hat{L} & 0 \\ 0 & 0 & 0 & 0 & 0 & \hat{N} \end{bmatrix}+\begin{bmatrix} \delta C_{11} & \delta C_{12} & \delta C_{13} & \delta C_{14} & \delta C_{15} & \delta C_{16} \\ \delta C_{12} & \delta C_{22} & \delta C_{23} & \delta C_{24} & \delta C_{25} & \delta C_{26} \\ \delta C_{13} & \delta C_{23} & \delta C_{33} & \delta C_{34} & \delta C_{35} & \delta C_{36} \\ \delta C_{14} & \delta C_{24} & \delta C_{34} & \delta C_{44} & \delta C_{45} & \delta C_{46} \\ \delta C_{15} & \delta C_{25} & \delta C_{35} & \delta C_{45} & \delta C_{55} & \delta C_{56} \\ \delta C_{16} & \delta C_{26} & \delta C_{36} & \delta C_{46} & \delta C_{56} & \delta C_{66} \end{bmatrix} \tag{A2}$$

where $\hat{A} = 3(C_{11} + C_{22})/8 + C_{12}/4 + C_{66}/2$, $\hat{C} = C_{33}$, $\hat{N} = (C_{11} + C_{22})/8 - C_{12}/4 + C_{66}/2$, $\hat{L} = (C_{44} + C_{55})/2$, and $\hat{F} = (C_{13} + C_{23})/2$.

Equations (1) and (A2) present a clear definition of what we call the "inherent" and "apparent" elastic moduli, respectively. The inherent moduli are $A, C, N, L,$ and, F from the elastic tensor with a vertical symmetry axis and the apparent moduli are $\hat{A}, \hat{C}, \hat{N}, \hat{L},$ and, $\hat{F}$ from the effective transversely isotropic part of the rotated elastic tensor.

We seek expressions for the period dependence of the phase speed for both Rayleigh and Love waves as well as the 2ψ azimuthal dependence for Rayleigh waves because these are the observations we make. This computation is based on the introduction of a transversely isotropic reference elasticity tensor composed of the depth dependent reference moduli $A_0, C_0, N_0, L_0,$ and, F_0. The code MINEOS will compute Rayleigh and Love wave phase speed curves for the reference model ($c_0^R(T), c_0^L(T)$). Then we define the effective transversely isotropic moduli relative to this reference:

$$\hat{A} = A_0 + \delta\hat{A}, \hat{C} = C_0 + \delta\hat{C}, \hat{N} = N_0 + \delta\hat{N}, \hat{L} = L_0 + \delta\hat{L}, \text{ and } \hat{F} = F_0 + \delta\hat{F}.$$

In this case, Montagner and Nataf present the required expressions for Rayleigh and Love wave phase speeds, which break into contributions from the reference moduli, the perturbation by the effective transversely isotropic (ETI) moduli relative to the reference moduli, and the azimuthally anisotopic (AA) moduli:

$$c_R(T, \psi) = c_0^R(T) + \delta c_R^{ETI}(T) + \delta c_R^{AA}(T, \psi) \quad \text{(A3)}$$

$$c_L(T) = c_0^L(T) + \delta c_L^{ETI}(T) \quad \text{(A4)}$$

where

$$\delta c_R^{ETI}(T) = \int_0^\infty \left\{ \delta\hat{A} \frac{\partial c_R}{\partial A}\bigg|_0 + \delta\hat{C} \frac{\partial c_R}{\partial C}\bigg|_0 + \delta\hat{L} \frac{\partial c_R}{\partial L}\bigg|_0 + \delta\hat{F} \frac{\partial c_R}{\partial F}\bigg|_0 \right\} dz \quad \text{(A5)}$$

$$\delta c_L^{ETI}(T) = \int_0^\infty \left\{ \delta\hat{N} \frac{\partial c_L}{\partial N}\bigg|_0 + \delta\hat{L} \frac{\partial c_L}{\partial L}\bigg|_0 \right\} dz \quad \text{(A6)}$$

$$\delta c_R^{AA}(T,\psi) = \int_0^\infty \left\{ \left(B_c \cos 2\psi + B_s \sin 2\psi\right) \frac{\partial c_R}{\partial A}\bigg|_0 + \left(G_c \cos 2\psi + G_s \sin 2\psi\right) \frac{\partial c_R}{\partial L}\bigg|_0 + \left(H_c \cos 2\psi + H_s \sin 2\psi\right) \frac{\partial c_R}{\partial F}\bigg|_0 \right\} dz \quad \text{(A7)}$$

The moduli B_c, B_s, G_c, G_s, H_c, and H_s are linear combination of the components of the azimuthally variable part of the elastic modulus matrix in Equation (A2), $\delta C_{\alpha\beta}^{AA}$, as follows:

$B_c = (\delta C_{11} - \delta C_{22})/2$, $B_s = \delta C_{16} + \delta C_{26}$, $G_c = (\delta C_{55} - \delta C_{44})/2$, $G_s = \delta C_{45}$, $H_c = (\delta C_{13} - \delta C_{23})/2$, and $H_s = \delta C_{36}$. Note that the azimuthally independent and 2ψ variations in surface wave phase speeds are sensitive only to 13 of the elements of the elastic tensor, and notably only the (1,6), (2,6), (3,6), (4,5) elements of the elastic tensor outside of the nine elements occupied under transverse isotropy. The other 8 elements of the elastic tensor ((1,4), (1,5), (2,4), (2,5), (3,4), (3,5), (4,6), (5,6)) are in the null space of surface wave phase speed measurements.

Montagner and Nataf present explicit formulas for the partial derivatives in Equations (A5) – (A7) in terms of normal mode eigenfunctions. Instead of using these expressions we recast the problem by computing the partial derivatives numerically which are computed relative to the reference model. The partial derivatives in the expression for the azimuthal term, $\delta c_R^{AA}(T,\psi)$, are equal to the partial derivatives of the azimuthally-independent terms (c_0^R, c_0^L) with respect to the corresponding transversely isotropic parameters (A, C, F, L, N). This feature facilitates the forward computation because the azimuthal dependence of surface

wave speeds can be computed using only the partial derivatives with respect to the five elastic parameters of a transversely isotropic medium, which can be achieved using the MINEOS code (*Masters et al*., 2007). **Figure A1** presents the sensitivity of Rayleigh and Love wave phase speeds at 20sec period to perturbations in L, N, C, A, and F as a function of depth. Love waves are sensitive almost exclusively to N, being weakly sensitivity to L, and completely insensitive to C, A, or F. In contrast, Rayleigh waves are sensitive to all of the parameters except N.

We represent the depth variation of the moduli by defining each on a discrete set of nodes distributed with depth and linearly interpolating the moduli between each node (**Fig. A2**). With this approach, we compute the partial derivatives using MINEOS by linear finite differences and convert the integrals to sums in Equations (A5) – (A7). The method is more accurate for Rayleigh than for Love waves and at longer rather than at shorter periods. For example, a constant 10% relative perturbation in the modulus N ($(\hat{N} - N_0)/N_0 = 0.1$, which is 5% in Vsh) across the entire crust produces an error in the computed Love wave phase speed of less than 0.1% except at periods less than 10 sec where it is only slightly larger. For Rayleigh waves, a similar constant 10% perturbation in L ($(\hat{L} - L_0)/L_0 = 0.1$, 5% in Vsv) results in an error less than 0.05% at all periods in this study. These errors are more than an order of magnitude smaller than final uncertainties in estimated model variables and, therefore, can be considered negligible.

FIGURE CAPTIONS

Figure A1. Example sensitivity kernels for Rayleigh and Love wave phase speeds at 20 sec period to perturbations in L, N, C, A, and F as a function of depth.

Figure A2. Illustration of the model discretization. At each grid point, the velocity profile is represented by a vertical set of nodes. Each model parameter is perturbed at each node to compute the depth sensitivity of surface wave data.

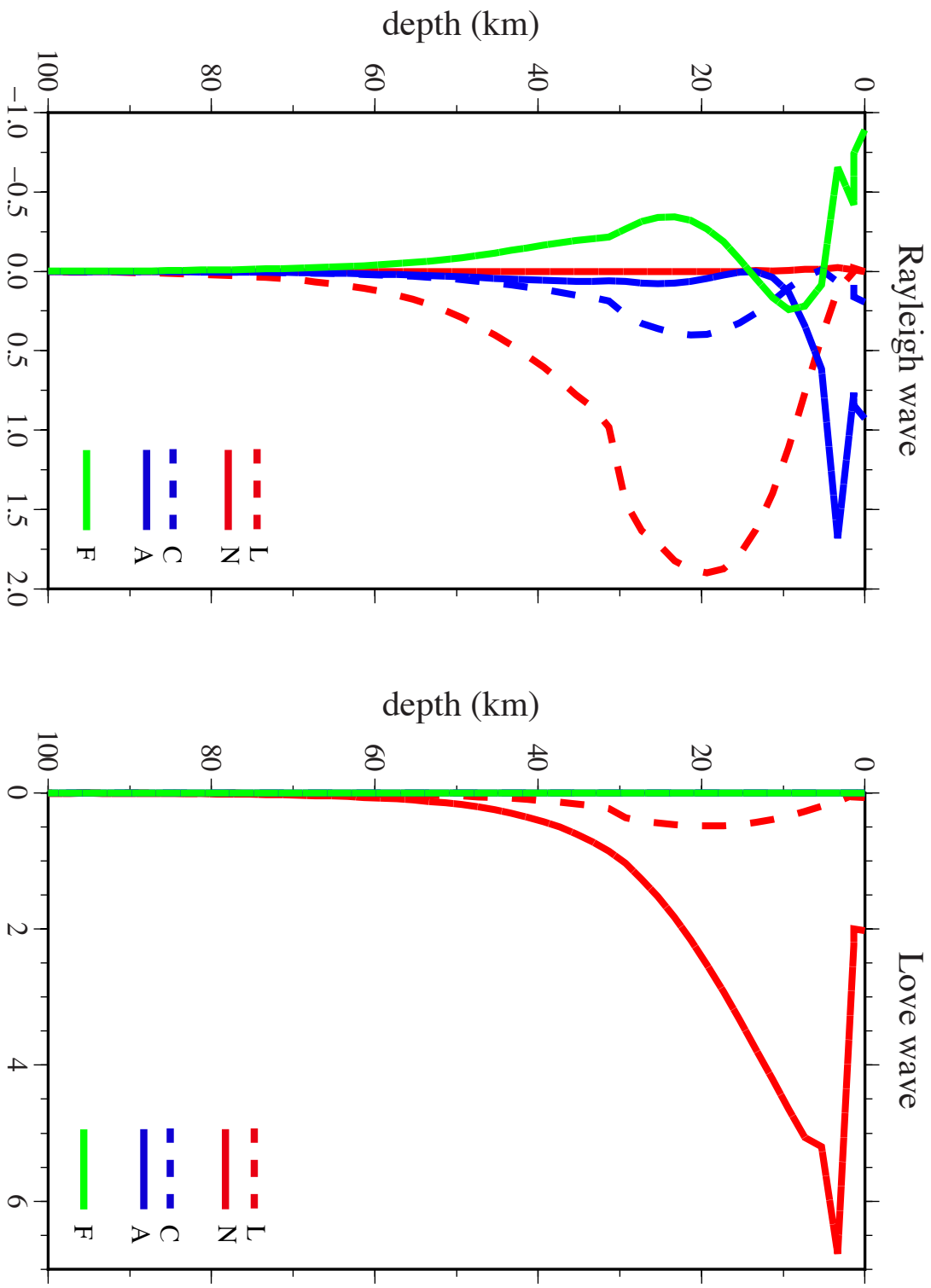
depth (km)
100
80
60
40
20
0
−1.0
−0.5
0.0
0.5
1.0
1.5
2.0
F
A
C
N
L
Rayleigh wave
depth (km)
100
80
60
40
20
0
0
2
4
6
F
A
C
N
L
Love wave

Figure A1

Figure A2